NOVA SCHOOL OF SCIENCE & TECHNOLOGY

DEPARTMENT OF MATERIALS SCIENCE

CATARINA VIEIRA MATOS

BSc in Micro and Nanotechnology Engineering

ATOMIC LAYER DEPOSITION OF THIN FILM CONDUCTORS FOR FLEXIBLE ELECTRONICS

MASTER IN MICRO AND NANOTECHNOLOGY ENGINEERING

NOVA University Lisbon

October, 2023

NOVA SCHOOL OF SCIENCE & TECHNOLOGY

DEPARTMENT OF MATERIALS SCIENCE

ATOMIC LAYER DEPOSITION OF THIN FILM CONDUCTORS FOR FLEXIBLE ELECTRONICS

CATARINA VIEIRA MATOS

BSc in Micro and Nanotechnology Engineering

Adviser: Ian Povey
Principal Scientist at Tyndall National Institute

Co-advisers: Pedro Miguel Cândido Barquinha
Associate Professor at NOVA University Lisbon

Examination Committee:

Chair: Hugo Manuel Brito Águas,
Associate Professor at NOVA University Lisbon

Rapporteur: Ricardo Manuel Fonseca Lopes da Silva,
PhD Researcher at CICECO

Member: Pedro Miguel Cândido Barquinha,
Associate Professor at NOVA University Lisbon

MASTER IN MICRO AND NANOTECHNOLOGY ENGINEERING

NOVA University Lisbon
October 2023

Atomic Layer Deposition of Thin Film Conductors for Flexible Electronics

Para as minhas irmãs.

ACKNOWLEDGMENTS

I would like to thank first and foremost the materials science department, which from the beginning of the course gave me the tools to jumpstart what has been a very fulfilling journey. From the first year's introduction to micro and nanotechnology classes to the final intricate nanofabrication classes, the INL internship opportunity, and now the chance to carry out part of this work at Tyndall National Institute, thank you.

This endeavour would not have been possible without my supervisors, Dr. Ian Povey and Professor Pedro Barquinha. I am very grateful for your guidance, knowledge, and inspiration. The stimulating talks about all the work possibilities as well as the continuous strive for good results were incredibly rewarding. I could not have undertaken this project without the help of so many professors, researchers and colleagues who dedicated their time and resources to provide results that constitute the bones of this dissertation. Special thanks to Jun Lin, James Connolly, Jonas Deuermeier, Ana Santa, Ana Rovisco, Hugo Águas, Joana Pinto, Daniela Gomes, João Pedro Veiga and Fernanda Carvalho. I would also like to extend my sincere thanks to Mariana Cortinhal who was always there every step of the way, to teach me, to answer all my questions and to allow a great part of the work to proceed the way it did. I really admire the enthusiasm and commitment she showed throughout the course of this work.

Agradeço agora a todos os meus colegas, principalmente aos que me acompanharam durante o decorrer da tese, nos almoços, no open-space e até nos laboratórios a vossa companhia tornou o trabalho mais agradável. Obrigada Apolo, Daniel, Duarte, Tiago e Nuno.

Quero ainda agradecer aos meus amigos por me aturarem e acompanharem durante tanto tempo, obrigada por todos os momentos que não me vou esquecer.

Por último (mas não menos importante) agradeço à minha família, aos meus pais por tudo o que fizeram para eu poder estar aqui hoje. Aos meus avós por me inspirarem. Às minhas tias, primas e irmãs pela vossa companhia. E finalmente ao meu maior companheiro, sempre presente, obrigada Tabarra.

This work received funding from the European Community's H2020 program under grant agreement no. 952169 (Synergy) and no. 101082283 (ERC-POC FLETRAD). This work was also funded by National Funds through the FCT - Fundação para a Ciência e a Tecnologia, I.P., under the scope of the projects UID/50025/2020-2023 and LA/0037/2020.

“I sit beside the fire and think
Of how the world will be
When winter comes without a spring
That I shall ever see.

For still there are so many things
that I have never seen:
in every wood in every spring
there is a different green.”
(J.R.R. Tolkien).

ABSTRACT

Flexible electronic circuits require thin conductive layers to act as contacts and interconnections. When using polymeric substrates, these layers must be deposited by low-temperature processes, which are essential to maintain the substrate's original properties. With the purpose of achieving low resistivity and high conformality to polyimide step structures, thin films consisting of titanium nitride (TiN) and aluminium-doped zinc oxide (AZO) were grown by plasma enhanced atomic layer deposition (PEALD), and thermal atomic layer deposition (ALD) respectively. The optimized process conditions included temperature, plasma composition, and duration for the TiN, and doping concentration for the AZO. The precursors/co-reactants used were tetrakis(dimethylamino)titanium (IV), $Ti[N(CH_3)_2]_4$ and N_2 or H_2/N_2 plasma for the TiN, and diethyl-zinc, $Zn(C_2H_5)_2$ and water for the ZnO, doped with cycles of trimethyl-aluminium, $Al(CH_3)_3$ and water for the AZO. The TiN depositions were performed at Tyndall National Institute, while the AZO was produced at CENIMAT.

The samples were characterized by Hall effect measurements, profilometry, X-ray photoelectron spectroscopy, X-ray diffraction, electron dispersive spectroscopy, transmission and scanning electron microscopy, and Raman spectroscopy. The best resistivities obtained were 1.67×10^{-3} Ω.cm for an AZO sample deposited at 180 ºC, with 1.94% atomic Al, and 3.07×10^{-3} Ω.cm for a TiN film produced at 300 ºC, with a 20 s H_2/N_2 plasma. TiN and AZO films grown on patterned polyimide over glass step structures at 250 ºC and 150/180 ºC respectively exhibited above 90% conformality, opening the possibility of their application in polymeric flexible electronic devices.

Keywords: Flexible electronics, conductive thin films, polyimide, TiN, AZO, PEALD, ALD, conformality.

RESUMO

Circuitos de eletrónica flexível exigem camadas finas e condutoras cujas funcionalidades incluem contactos e ligações elétricas. No caso da utilização de substratos poliméricos, estas camadas devem ser depositadas por processos a baixa temperatura, de forma a manter as propriedades originais do substrato. Tendo o objetivo de obter baixa resistividade e elevada conformabilidade com estruturas tipo "degrau" de poliamida, filmes finos de nitreto de titânio (TiN) e de óxido de zinco dopado com alumínio (AZO), foram crescidos por deposição de camadas atómicas assistida por plasma (PEALD), e deposição térmica de camadas atómicas (ALD), respetivamente. As condições de processo otimizadas incluíram temperatura, composição e duração do plasma, para o TiN, e concentração do dopante, para o AZO. Os precursores/co-reagentes utilizados foram o titânio (IV) dimetilamida, $Ti[N(CH_3)_2]_4$ e plasma de N_2 ou H_2/N_2, em relação ao TiN, e dietilzinco, $Zn(C_2H_5)_2$ e água formando ZnO, dopado com ciclos de trimetilaluminio, $Al(CH_3)_3$ e água, para obter AZO. As deposições do TiN decorreram no Tyndall National Institute, enquanto as de AZO foram realizadas no CENIMAT.

As amostras foram caracterizadas por medidas de efeito de Hall, elipsometria, espetroscopia de fotoeletrões excitados por raios X, difração de raios X, espetroscopia dispersiva de energia, microscopia de transmissão e varrimento, e espetroscopia Raman. As melhores resistividades obtidas foram 1.67×10^{-3} Ω.cm, para uma amostra de AZO depositada a 180 ºC, com 1.94% atómica de Al, e 3.07×10^{-3} Ω.cm, para um filme de TiN produzido a 300 ºC, com um plasma de 20 s de H_2/N_2. Filmes de TiN e AZO crescidos sobre estruturas padronizadas com degraus de poliamida sobre vidro, a 250 ºC e 150/180 ºC revelaram conformabilidade superior a 90%, tornando possível a sua aplicação em dispositivos poliméricos de eletrónica flexível.

Palavras chave: Eletrónica flexível, películas finas e condutoras, poliamida, TiN, AZO, PEALD, ALD, conformabilidade.

CONTENTS

MOTIVATION AND OBJECTIVES **1**

1. INTRODUCTION **2**

1.1 Atomic Layer Deposition 2

1.1.1 ALD of Titanium Nitride 3

1.1.2 ALD of Aluminium Doped Zinc Oxide 5

2. MATERIALS AND METHODS **7**

2.1 Thin Film Deposition 7

2.2 Thin Film Characterization 8

3. RESULTS AND DISCUSSION **9**

3.1 TiN Film Growth 9

3.2 TiN Structure and Composition 11

3.2.1 X-ray Photoelectron Spectroscopy 11

3.2.2 X-ray Diffraction 14

3.3 TiN Electrical Properties 16

3.4 AZO Film Growth 17

3.5 AZO Structure and Composition 18

3.5.1 Energy Dispersive Spectroscopy 18

3.5.2 X-ray Diffraction 19

3.6 AZO Electrical Properties 20

3.6.1 Post-treatment Study of the AZO samples 23

3.6.1.1 UV-Ozone 23

3.6.1.2 Rapid Thermal Annealing 24

3.7 Benchmarking of TiN and AZO Electrical properties 25

3.8 Conformality Study 26

3.8.1 TiN Conformality 26

3.8.2 AZO Conformality 27

3.8.3 Final considerations on TiN and AZO conformality 28

4. CONCLUSIONS AND FUTURE WORK **29**

5. REFERENCES **31**

APPENDIX **33**

A.1 TiN PEALD Recipe Information 33

A.2 AZO ALD Recipe 34

A.3 Sample List 37
A.4 Polyimide Substrates 38
A.5 TiN Thickness Calculation Method 40
A.6 XPS Models 42
A.7 FIB-SEM 44
A.8 UV-Ozone and RTA post-treatment plots 45

LIST OF FIGURES

Figure 1: Schematic of Atomic Layer Deposition (ALD) and Plasma Enhanced ALD binary reaction mechanism. Adapted from [3]. 2
Figure 2: Growth per cycle versus deposition temperature and related phenomena. Adapted from [2]. 3
Figure 3: Cross-section TEM image of a PEALD TiN film covering a deep structure. Adapted from [4]. 3
Figure 4: Schematic diagram of PEALD growth process for TiN films. 4
Figure 5: Representation of a super cycle of an AZO ALD process. Adapted from [16]. 6
Figure 6: Brightfield TEM images of TiN sample 300H20b-Capped, with identification of the layers and their thickness from surface to substrate: Al_2O_3 capping with 3.6 ± 0.6 nm, TiN with 39.4 ± 0.4 nm, Al_2O_3 with 4.8 ± 0.1 nm and SiO_2 with 1.8 ± 0.1 nm. 9
Figure 7: XPS %Ti and %Al depth profile of selected TiN samples. 9
Figure 8: Growth per Cycle of TiN samples using 15 s of N_2 plasma, 15 s of H_2/N_2 plasma and 20 s of H_2/N_2 plasma with the "booster" condition. 10
Figure 9: XPS elemental depth profile of the TiN sample 300H20b-Capped as a function of Ar^+ sputter time. 12
Figure 10: XPS detailed scan of Ti 2p peak at the surface of the 300H20b sample and after 8 minutes of Ar^+ sputtering. Includes fitting of the components Ti-N, Ti-N-O, and Ti-O, forming the envelope in brown, and raw data in red. 12
Figure 11: XPS N1s peak from the TiN sample 300H20b native surface and after 8 minutes of Ar^+ ion sputtering. 13
Figure 12: XPS atomic concentration of the Ti 2p components: Ti-N, Ti-N-O, and Ti-O for the 300H20b Al_2O_3 capped and uncapped samples. 14
Figure 13: XRD results of samples with a) different plasma composition and duration and b) different deposition temperatures: 300 ºC, 250 ºC and 200 ºC, with identification of reference peaks of TiC (111) at 35.9º, TiN (111) at 36.5º, TiO (111) at 37.4º, TiC (200) at 41.7º, TiN (200) at 42.5º and TiO (200) at 43.4º [6,30]. 15
Figure 14: XRD spectra of samples with different deposition number of cycles. 15
Figure 15: Raman spectrum of sample 300H20b-1500. 15
Figure 16: TiN resistivity as a function of a) deposition temperature and b) plasma duration. 16
Figure 17: Resistivity of TiN samples as a function of the number of cycles of the PEALD deposition. 17
Figure 18: Effect of deposition temperature and DEZ:TMA cycle ratio on the Growth Per Cycle of AZO samples. 18
Figure 19: EDS spectrum of sample AZO180-59:1 with identified element emission energies. 19
Figure 20: EDS measured Aluminium atomic concentration (%Al) of AZO samples as a function of deposition temperature and DEZ:TMA ratio. 19
Figure 21: XRD spectra of samples AZO150-59:1 and AZO180-59:1, with inset of peaks (100), (002) and (101). 19
Figure 22: Effect of DEZ:TMA ratio on ρ, μ and N for AZO thin films produced at a temperature of 150ºC. 20
Figure 23: Effect of DEZ:TMA ratio on ρ, μ and N for AZO thin films produced at a temperature of 180ºC. 21
Figure 24: Resistivity (ρ) of AZO samples as a function of DEZ:TMA ratio and temperature. 21

Figure 25: a) Carrier Concentration and b) Mobility of AZO samples as a function of DEZ:TMA ratio and temperature. 22
Figure 26: UV-Ozone post-treatments performed on sample AZO180-69:1 for 5, 10, 15 and 30 minutes, with the a) resistivity and b) carrier concentration of measurements after deposition, after UV-O3 treatments, 6 days and 2 months later. 23
Figure 27: a) Resistivity and b) Carrier concentration of replicas of sample AZO180-129:1 as deposited, after 15 minutes of UV-O3 and remeasured 3 days later, one left at atmospheric pressure and the other left in low vacuum inside the hall effect system. 24
Figure 28: Resistivity as a function of N_2 RTA treatment time for a) AZO180-99:1 sample at 999 mbar, and b) AZO180-59:1 sample at 100 mbar. 25
Figure 29: Resistivity as a function of deposition temperature. Includes TiN and AZO literature values, as well as the present work's lowest resistivities for each deposition temperature, blue for TiN and green for AZO. 25
Figure 30: EDS elemental maps and SEM image of 600 cycles of TiN and 500 cycles of Al_2O_3 on a PI/glass step patterned substrate, at 250 ºC. 26
Figure 31: EDS elemental maps and SEM image of 600 cycles of TiN and 500 cycles of Al_2O_3 on a PI/glass step patterned substrate, at 300 ºC. 26
Figure 32: Conformality of Al_2O_3 and TiN layers as a function of substrate and temperature. 27
Figure 33: SEM images of a) PAZO150-69:1 and b) PAZO180-59:1 deposited on PI/glass step patterned substrates. 28
Figure 34: Conformality of AZO as a function of substrate and temperature. 28
Figure 35: Representative image of the trench/step patterned PI on glass substrate. 38
Figure 36: SEM image of a cross section of sample PAZO150-69:1 38
Figure 37: SEM cross section image of a sample P250H20b-600. 39
Figure 38: XPS Titanium signal as a function of Ar^+ sputter time, containing linear fittings with equal slope, and half maximum intersection dashed lines with corresponding colours. 40
Figure 39: XPS Aluminium signal as a function of Ar^+ sputter time, containing linear fittings with equal slope, and half maximum intersection dashed lines at 9.6% and 20.5%. 41
Figure 40: XPS Ti 2p detailed scan of sample 300H20b-Capped after 5 minutes of Ar^+ sputtering with 5 kV, using peak fitting with model described in Table 14. The raw data is in red, the components are identified in the table on the right, and together they form the envelope in brown. 43
Figure 41: XPS C 1s detailed scan of sample 300H20b-Capped after 5 minutes of Ar^+ sputtering with 5 kV, using peak fitting with model described in Table 15. The raw data is in red, the components are identified in the table, and together they form the envelope in brown. 43
Figure 42: SEM image of a cross-section of sample AZO180-59:1 milled with FIB. 44
Figure 43: a) Mobility of AZO180-69:1 samples, as deposited, after UV-O_3 treatments of 5, 10, 15 and 30 minutes, remeasured 6 days and 2 months later, b) Mobility of AZO180-129:1 samples as deposited, after 15 min UV-O_3 post-treatment, and 3 days later. 45
Figure 44: a) Carrier concentration and b) mobility of N_2 RTA post-treatments to sample AZO180-99:1, at 300 ºC and 999 mbar. 45

LIST OF TABLES

Table 1: Literature of selected TiN PEALD conditions and resulting film properties. 5
Table 2: Literature of selected AZO ALD conditions and resulting film properties. 6
Table 3: PEALD deposition conditions for the initial TiN thin films. 7
Table 4: Thermal ALD deposition conditions for the AZO thin films. 8
Table 5: Thickness of TiN samples measured with XPS depth profiles. 9
Table 6: XPS average atomic concentration of Ti, N, O, C, and other elements obtained from the depth profiles. 11
Table 7: XPS Ti 2p and C 1s peak components model fitting results calculated with *casaxps*. 13
Table 8: Profilometry thickness of AZO samples. 18
Table 9: AZO structural, compositional, and electrical properties. 22
Table 10: Thickness measurements of TiN and Al_2O_3 layers from SEM images. 27
Table 11: Thickness of AZO films measured from SEM images. 28
Table 12: ALD conditions on the *R200 Advanced Picosun* system. 33
Table 13: List of samples deposited by PEALD and ALD. 37
Table 14: XPS model for fitting of the Ti 2p peak with energy, area and FWHM restrictions. 42
Table 15: XPS model for fitting the N 1s and C 1s peak with energy, area and FWHM restrictions. 42

ACRONYMS

ALD	Atomic Layer Deposition
AZO	Aluminium-doped Zinc Oxide
CENIMAT	Centro de Investigação de Materiais
CMOS	Complementary Metal-Oxide-Semiconductor
CVD	Chemical Vapour Deposition
EDS	Energy Dispersive Spectroscopy
FCT	Faculdade de Ciências e Tecnologia
FIB	Focused Ion Beam
FWHM	Full Width Half Maximum
GPC	Growth per Cycle
ITO	Indium Tin Oxide
LED	Light Emitting Diode
MIM	Metal-Insulator-Metal
PEALD	Plasma Enhanced Atomic Layer Deposition
PI	Polyimide
PVD	Physical Vapour Deposition
SEM	Scanning Electron Microscopy
TDMAT	Tetrakis(dimethylamino)titanium (IV)
TEM	Transmission Electron Microscopy
TMA	Trimethylaluminium
UNL	Universidade Nova de Lisboa
UV	Ultraviolet
XPS	X-ray Photoelectron Spectroscopy
XRD	X-ray Diffraction

SYMBOLS

Å	Angstrom
N	Carrier Concentration
μ	Mobility
ρ	Resistivity
T	Temperature
t	Thickness
λ	Wavelength

MOTIVATION AND OBJECTIVES

Scientific interest in flexible electronics as a means of self-sustainable smart platforms has been growing as a result of their many advantages, including large area, light weight, bendability, portability, and lower costs associated with roll-to-roll processes [1]. Flexible electronic devices require thin and conformal conducting layers, working as contacts and circuit interconnections to be deposited onto flexible substrates. In the case of polymeric substrates, the conducting films must be fabricated by low-temperature processes, namely below the glass transition temperature of the substrate material (~350 ºC for polyimide) for it to maintain its original properties throughout the deposition process [1].

Atomic Layer Deposition is a thin film depositing gas-phase technique that allows very precise thickness control, high conformality to complex three-dimensional structures, and low process temperature, compared with Chemical Vapour Deposition (CVD) techniques [2]. Besides, since its establishment ALD has been used to research a vast range of materials and it is currently used in the CMOS microelectronics industry to deposit high-k gate dielectrics and metal gates [2]. Since metal ALD is still challenging and materials such as metal nitrides and metal oxides show consistently good results, both in terms of low resistivity and good conformality [3], this work focused on ALD of Titanium Nitride and Aluminium-doped Zinc Oxide.

The objective of this work was to develop conductive layers of Plasma Enhanced Atomic Layer Deposition based thin films of TiN and thermal ALD based films of AZO, to ultimately deposit them on step patterned polyimide (PI) covered glass substrates, to study their conformality. To enable this, the resistivity was improved considering the effects of deposition conditions, such as temperature, plasma pulse duration, and plasma composition for the TiN process, and temperature and aluminium doping concentration for the AZO process. Post treatments, including UV-Ozone and Rapid Thermal Annealing, were studied as low-thermal-budget (<300 ºC) tools to further reduce the AZO thin film resistivity.

1. INTRODUCTION

1.1 Atomic Layer Deposition

Atomic Layer Deposition is a gas phase deposition technique, derived from CVD, that employs surface reactions to generate thin films on a substrate [2]. Thermal ALD requires heating the substrate during the deposition to provide the necessary activation energy to bind the chemical reactants (a precursor of the wanted material and a co-reactant) on the substrate surface, and in a layer-by-layer sequence obtain a uniform film of the intended material [2]. In this process, to avoid gas phase reactions, precursors are injected separately between purge cycles of an inert gas (usually N_2) which extracts all excess reactant and by-products from the chamber (Figure 1). Unlike CVD processes, energetically favourable surface chemistry and the avoidance of gas phase reactions ensures that all available surface sites react in a self-limiting manner [2]. This self-limiting nature of ALD is what allows the fabrication of very pure, conformal, and pin-hole free films, with a precise thickness, optimal for electrically demanding applications [2].

When plasma is used during the co-reactant pulse (PEALD), it causes the formation of highly reactive radicals of the co-reactant gas, which easily bind to the substrate groups. Therefore, this ALD variant provides more reactive co-reactant species without requiring as high a temperature as thermal ALD. This often allows the production of denser films, with enhanced electrical properties and lower roughness, using less reactive precursors [2,3]. On the other hand, plasma uniformity can be difficult to achieve and there is a high probability of recombination of the radical plasma species and their incorporation in the formed film, compromising the conformality, especially in high aspect ratio trenches and vias [3].

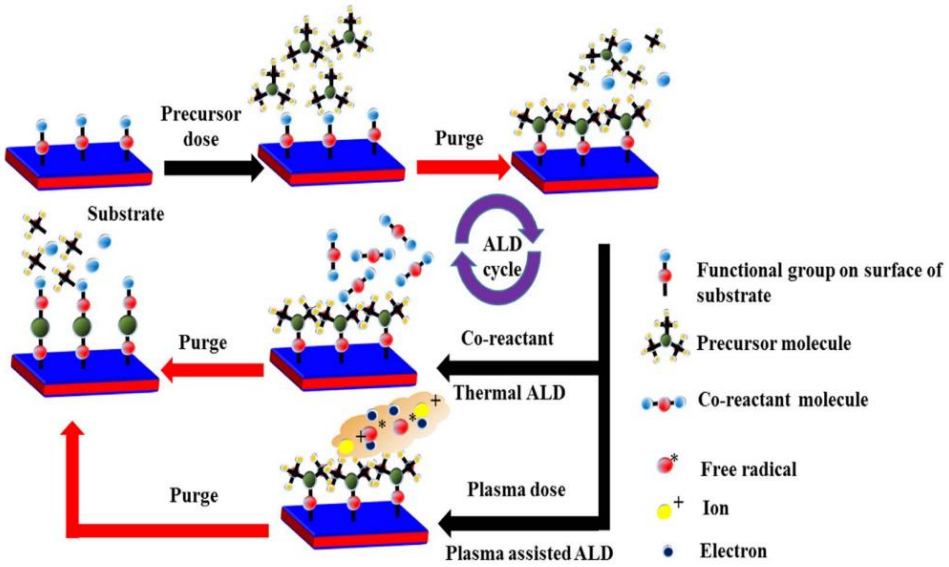

Figure 1: Schematic of Atomic Layer Deposition (ALD) and Plasma Enhanced ALD binary reaction mechanism. Adapted from [3].

Besides the regular ALD process (repetition of an $(AB)_m$ sequence, A for precursor and B for co-reactant, m times), this technique allows multi-compound materials to be produced using a super cycle process, where two or more individual regular cycles are combined, for instance in a $((AB)_m(CB)_n)_x$ cyclic sequence [2]. This makes it straightforward to deposit nanolaminates and easily add dopants with ALD [2].

For each process, there is a temperature window where the Growth Per Cycle (GPC) is constant, which is the optimal temperature range for an ideal ALD deposition (Figure 2). Outside this temperature window, the GPC may vary due to different phenomena, it can decrease due to species desorption or low reactivity due to low thermal energy, and it can increase due to the gas phase decomposition of the precursor, or co-reactant, or due to condensation of these species on the substrate, in CVD-like film growth (Figure 2).

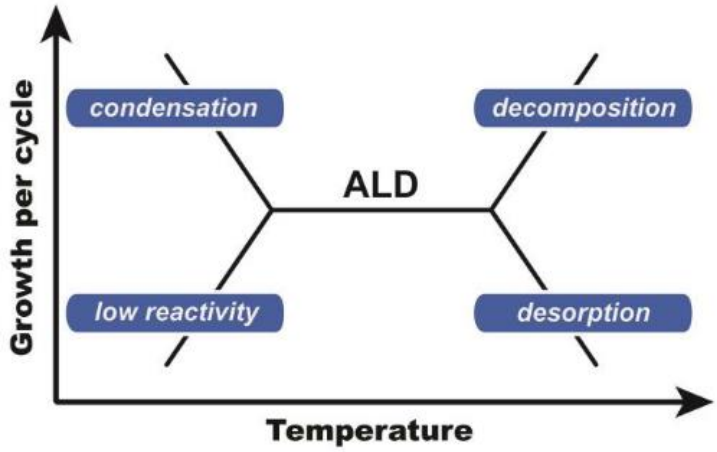

Figure 2: Growth per cycle versus deposition temperature and related phenomena. Adapted from [2].

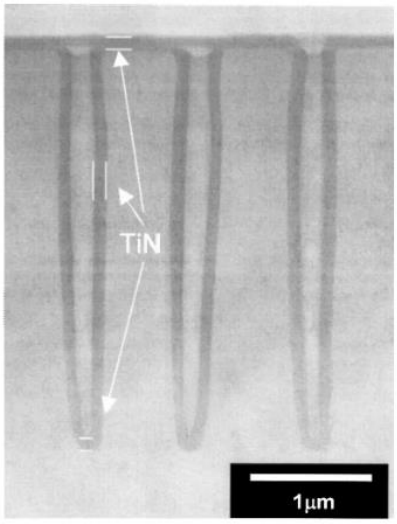

Figure 3: Cross-section TEM image of a PEALD TiN film covering a deep structure. Adapted from [4].

The precursors are a very important aspect of ALD, since this is a chemical technique involving chemical reactions between compounds, which requires fast precursor chemisorption and effective bond formations [2]. After choosing the right precursor and co-reactant to deposit a thin film of a certain material, the minimum requirement for obtaining uniform films with this technique is a reagent flux that reaches and binds to the full substrate area, during the precursor pulse duration [2]. In fact, the challenges of this technique come not only from the complexity of the chemical reactions, but also from the large number of deposition parameters (pulse and purge times, temperature, pressure, gas flow rates, and others), that can affect the resulting film's properties, so, it is crucial to optimize an ALD process.

To improve this technique's long deposition times spatial ALD reactors can be used. Instead of separating the reaction steps in time, the substrate can move from separated compartments where the distinct reaction steps are occurring, reducing the overall deposition duration [2].

While uniformity is evaluated by the film coverage of the planar surface, meaning its thickness variance throughout the surface area, the conformality represents the film coverage of 3D features [2]. The potential of this technique is reached in applications requiring highly conformal layers to complex shaped structures, such as in high aspect ratio trenches (Figure 3) used, for instance, in trench MIM capacitors.

1.1.1 ALD of Titanium Nitride

Titanium Nitride is a metallic nitride, with high thermal stability and chemical resistance, typically used for protective coatings and anti-diffusion barriers between metal electrodes and adjacent layers [5]. Furthermore, this material can have low enough resistivity to be applied as a gate electrode in some microelectronic applications (trench MIM capacitors and 3D memory devices) [5]. Conventional fabrication techniques

include PVD and CVD processes, however, these present poor step coverage and high temperature limitations respectively [5].

As an alternative TiN can be deposited by thermal ALD, but usually better film properties are obtained by PEALD [6]. The PEALD process follows the repetition of a normal ALD cycle of four steps, first the injection of a titanium precursor, then a purge of an inert gas (N_2 or Ar), followed by a plasma pulse of the co-reactant species, and finally another purge (Figure 4).

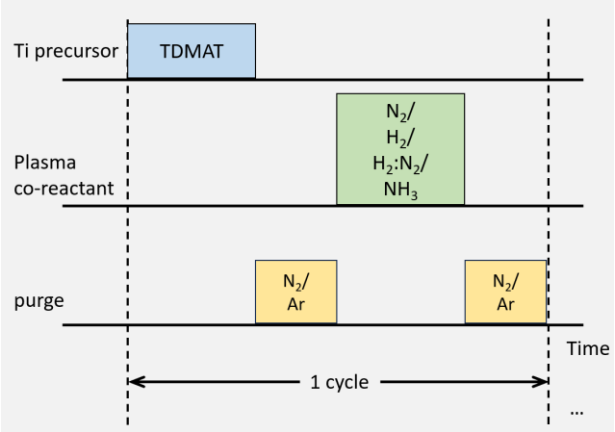

Figure 4: Schematic diagram of PEALD growth process for TiN films.

One of the most used titanium precursors is titanium tetrachloride ($TiCl_4$) [5]. This halide compound has a high reactivity, vapor pressure and thermal stability and produces highly crystalline, low resistivity films [7]. However, it requires high process temperatures, which are not compatible with sensitive substrates, and may form chlorine impurities which are corrosive and can degrade the long-term reliability of the microelectronic devices, as well as the deposition tools [7]. The usual alternative is the metalorganic tetrakis(dimethylamido)titanium (IV) ($Ti[N(CH_3)_2]_4$, TDMAT), which promotes a higher growth rate, less crystalline and more porous structure, with a higher resistivity, partly due to carbon incorporation, explained by this precursor's low decomposition temperature [5].

The plasma gas is usually one of the following: nitrogen (N_2), hydrogen (H_2), forming gas (H_2/N_2) or ammonia (NH_3). The lowest resistivities are associated with processes using ammonia due to not only, an optimum N:H ratio that provides advantages from both plasma gases, namely the higher chemical reactivity of the hydrogen radicals, and physical reactivity of the nitrogen radicals, but also because NH· radicals are more reactive than N· and H· radicals [7].

The chemical reactions during this PEALD deposition start with a transamination reaction by the exchange of amine radicals between the precursor species, TDMAT, and the surface species' hydrogen, in the -NH surface sites (*) during the precursor pulse, with a release of gaseous dimethylamine (Equation 1.1) [8]. During the co-reactant pulse, there is an amine elimination reaction of the remaining amine groups bound to the Ti atom centre, leaving behind new -NH groups for the next precursor pulse (Equation 1.2) [8]. In truth, this is a complex chemical system and there are many reaction possibilities, including the ones leading to the incorporation of carbon in the film (transposition reactions) [8].

$$2NH^*\,(s) + Ti[N(CH_3)_2]_4\,(g) \rightarrow N_2Ti(N(CH_3)_2)_2^*\,(s) + 2HN(CH_3)_2\,(g) \quad (1.1)$$

$$N_2Ti(N(CH_3)_2)_2^*\,(s) + \begin{Bmatrix} NH_3 \\ N_2 \\ H_2 \end{Bmatrix} (g)\ Plasma \rightarrow N_2TiNH_2^*(s) + \begin{Bmatrix} HN(CH_3)_2 \\ CH_3NH_2 \\ CH_4 \end{Bmatrix} (g) + \begin{matrix} other \\ hydro- \\ carbons \end{matrix} \quad (1.2)$$

Literature conditions and properties of PEALD TiN processes using N_2 and/or H_2 plasma are displayed in Table 1. The lowest resistivity reaches 115 μ.Ω.cm [7], due to the following important conditions: very low reactor pressure (0.001-0.22 Torr) and low gas flow rates (10 sccm), which lead to a higher ion flux toward the substrate that stimulates the film's densification and crystallization, short precursor pulses (0.3 s) limit the

impact of the TDMAT decomposition on the growth rate [5], and minimize the film porosity, thereby reducing oxidation [9], a temperature of 300 ºC provides the necessary energy for the chemical reactions to occur, 20 s plasma pulses efficiently maximizes the removal of the precursor ligands by the plasma radicals, without leading to excessive oxygen contamination [5], and 10 s purges decrease any CVD-like deposition [2]. A low resistivity TiN must be close to stoichiometric with minimum levels of carbon and oxygen contamination, C-H and Ti-O bonds respectively, as these are thought to decrease film stability and act as scattering centres, by accumulating at grain boundaries, respectively [7].

Table 1: Literature of selected TiN PEALD conditions and resulting film properties.

Plasma Gas	**T (ºC)**	**Plasma Power (W)**	**Cycle times (s)** TDMAT/p/Plasma/p (p for purge)	**GPC (Å.cycle^{-1})**	**t (nm)**	**ρ (μΩ.cm)**	**Ref.**
N_2	200	300	0.2/6/10/20	0.6	50.0	5000	[6]
	250	300	5/5/20/5	3.8	19.0	300	[4]
		500	1.5/6/20/3	1.0	67.5	130	[10]
	300	200	0.3/10/20/10	0.7	30.0	115	[7]
		300	0.3/10/20/10	0.7	25.0	120	[5]
H_2/N_2	250	300	5/5/20/5	3.9	19.5	700	[4]
H_2	150	600	0.2/1.5/2/1.5	0.4	10.0	201	[8]
	175	250	3/35/20/35	0.3	8.2	200	[11]
	200	250	1/3/1/3	0.4	40.0	200	[12]
N_2; H_2; NH_3	250	200	5/10/20/10	2.0	20.0	1000-1500	[13]

1.1.2 ALD of Aluminium Doped Zinc Oxide

Zinc Oxide (ZnO) is intrinsically an n-type semiconductor with a wide direct bandgap (3.36 eV) that is used as a transparent conductive oxide in diverse optoelectronic applications such as solar cells, LEDs and displays [14]. This material's conductivity can be improved by extrinsic dopants, if they have a different oxidation number than Zn atoms they can provide extra electrons (e.g. Al), and by intrinsic donors from lattice defects in the structure, like oxygen vacancies [15]. Aluminium-doped Zinc Oxide can be deposited by a variety of methods including sputtering, pulsed laser deposition, sol-gel, CVD and ALD [14]. AZO has been intensively researched as a substitute of ITO, which is the conventional currently used TCO, however it presents a series of challenges including toxicity, scarcity, lack of thermal stability and flexibility, which AZO can answer [16].

ALD of AZO consists in a sequence of "n" binary cycles of a zinc precursor, usually diethyl-zinc ($Zn(C_2H_5)_2$, DEZ), and an oxidant co-reactant such as water (H_2O), forming zinc oxide, followed by a single binary cycle of trimethyl-aluminium (TMA) and water, forming aluminium oxide (Al_2O_3), resulting in a super cycle process (Figure 5) [16]. By changing the number of DEZ/H_2O cycles to every TMA/H_2O cycle ("n") one can control the aluminium dopant concentration (%Al), to optimize the film's electrical properties [16].

The chemical reactions occurring during the deposition of AZO, on silicon substrates, start with a pulse of DEZ, which adsorbs to the hydroxyl groups (-OH) and releases one of its ethyl groups (CH_3CH_3) (Eq 2.1) [17]. After this step, there is a purge of all byproducts, followed by a water pulse that substitutes the leftover ethyl group by a hydroxyl group, and can react with a new DEZ molecule in the next cycle (Eq 2.2) [17]. Between the DEZ/H_2O cycles there is one TMA/H_2O cycle with a similar reaction. In this case, there is

a release of one of the TMA's methyl groups (in the form of CH_4) during the TMA pulse (Eq 3.1), and the substitution of the remaining methyl groups in the subsequent water pulse (Eq 3.2) [17].

$$-Si-OH^{*}+Zn(C_2H_5)_2 \rightarrow -Si-O-Zn-(CH_2CH_3)^{*}+CH_3CH_3 \quad (2.1)$$

$$-Si-O-Zn-(CH_2CH_3)^{*}+H_2O \rightarrow -Si-O-Zn-OH^{*}+CH_3CH_3 \quad (2.2)$$

$$-Si-O-Zn-OH^{*}+Al(CH_3)_3 \rightarrow -Si-O-Zn-O-Al(CH_3)_2^{*}+CH_4 \quad (3.1)$$

$$-Si-O-Zn-O-Al(CH_3)^{*}+H_2O \rightarrow -Si-O-Al-OH^{*}+CH_4 \quad (3.2)$$

ALD of AZO has been carried out at a wide temperature range (60 ºC-300 ºC [18]), however, the ALD window is more strictly bound to temperatures near 150 ºC (140 ºC-180 ºC [17]). The limiting factor is the ZnO, and not the Al_2O_3, because Al_2O_3 has a wider ALD temperature window [3]. Below 150 ºC, the ZnO growth rate decreases, because of the kinetic barrier that prevents complete surface reactions, while above this temperature the growth rate also decreases, because of both a decrease in hydroxyl surface coverage, caused by water desorption, reducing adsorption sites, and also an increased DEZ desorption [17].

Most studies of AZO ALD reach the lowest resistivities for an atomic %Al between 1.9% and 3% (Table 2). These dopant contents are obtained with different DEZ:TMA ratios, depending on each deposition conditions, the reactor used, the flows, the pulse durations, etc. Below this %Al range the dopant effect is very low, and the film has undoped-ZnO typical behaviour, whereas above it this concentration surpasses the solubility limit, forming secondary phases that affect the film's crystallinity, and degrade its electrical properties [18]. Studies of AZO ALD deposited at different temperatures reveal that the resistivity decreases until 240 ºC-250 ºC, increasing for higher temperatures [16].

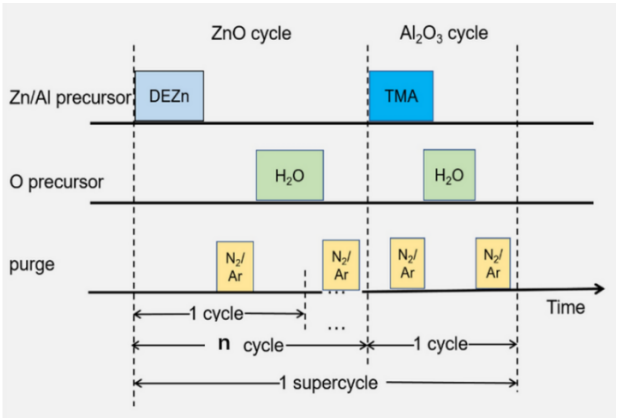

Figure 5: Representation of a super cycle of an AZO ALD process. Adapted from [16].

Table 2: Literature of selected AZO ALD conditions and resulting film properties.

T (ºC)	DEZ: TMA	Cycle times (s) DEZ/p/TMA/p/H_2O/p (p for purge)	t (nm)	GPC (Å.cycle^{-1})	Al (%)	ρ (Ω.cm)	μ (cm^2.V^{-1}.s^{-1})	N (cm^{-3})	Ref.
150	100	0.5/8/0.15/5/0.5/4	43.3	2.1	1.98	6.65×10^{-3}	7.1	1.38×10^{20}	[19]
150	20	0.25/p/0.25/p/0.25/p	97.3	1.9	3.00	4.40×10^{-3}	8.4	1.70×10^{20}	[20]
160	19	0.04/1/0.04/1/0.02/2	214.0-233.0	-	2.50	6.33×10^{-3}	7.3	1.34×10^{20}	[21]
200	19	2/5/2/5/2/5	42.1	2.2	1.90	3.20×10^{-3}	14.3	1.40×10^{20}	[22]
200	20	2/5/0.1/5/2/5	23.2	1.2	2.10	1.70×10^{-3}	7.6	4.70×10^{20}	[23]
220	24	0.025/p/0.02/p/0.015/p	71.2	1.0	2.17	8.33×10^{-4}	17.4	4.32×10^{20}	[16]
250	30	0.015/p/0.015/p/H_2O/p	180.0	1.4	1.10	6.30×10^{-4}	3.5	2.60×10^{21}	[24]

2. MATERIALS AND METHODS

This chapter describes the systems and conditions used in the deposition and characterization of the TiN and AZO thin films, fabricated throughout the course of this work.

2.1 Thin Film Deposition

An *ALD R200 Advanced Picosun* system at Tyndall National Institute was used for the TiN PEALD depositions (A.1). The substrates included a Si (100) wafer and a 1cm^2 square glass, the latter being cleaned in sequence with acetone, isopropyl alcohol, and water, and dried with N_2 before each deposition. The precursor used was TDMAT, heated to 85-90 ºC to increase its vapor pressure, and the plasma gases were N_2 and H_2/N_2. The plasma power used for all PEALD depositions was 1.8 kW. In the first 10 depositions, the plasma and temperature conditions were varied, as described in Table 3, where the samples are named firstly by their respective deposition temperature, in ºC, then by the plasma gas (N for N_2 and H for H_2/N_2), and finally, the plasma duration, in seconds. The first 10 TiN sample depositions were all 400 cycles long and included an Al_2O_3 underlayer of 23 nm, directly on the substrates, to have a similar layer composition as the initial contact surface for the TiN thin films. Sample 300H20b uses a booster of 600 sccm N_2 and 2 s precursor pulse, instead of the 0.3 s used for the other samples. This sample also includes an underlayer of 4.8 nm of Al_2O_3. Using the conditions of sample 300H20b, a thickness series of 400, 600, 1000, and 1500 cycles and another temperature series (200 ºC, 250 ºC and 300 ºC), were also deposited (A.3). Additionally, a capping layer of 20 cycles of Al_2O_3 was deposited on a sample equal to 300H20b, which was named 300H20b-Capped.

Table 3: PEALD deposition conditions for the initial TiN thin films.

TiN Sample	**250N 15**	**275N 15**	**300N 10**	**300N 15**	**300N 20**	**250H 15**	**275H 15**	**300H 10**	**300H 15**	**300H 20**	**300H 20b**
Plasma Gas	N_2					H_2/N_2 (1/10)					
T (˚C)	250	275	300			250	275	300			
Plasma Dur. (s)	15		10	15	20	15		10	15	20	

Regarding the AZO thermal ALD depositions, a *Beneq TFS-200* reactor at CENIMAT was employed to produce thin films of varying $ZnO:Al_2O_3$ ratios, and deposition temperatures (Table 4), with the following pulse times for each super cycle: 0.5 s of DEZ, 10 s N_2 purge; 0.15 s of TMA;10 s N_2 purge; 0.15 s of H_2O; 10 s purge. A temperature of 150 ºC and the DEZ/TMA ratios were chosen from conclusions of a previous work using the same reactor [19], where the 100:1 ratio presented the best electrical properties. A higher temperature of 180 ºC was also included in the present study. Si (100) wafer and corning glass 5 cm × 5 cm substrates were used, after a cleaning process of 10 minutes of ultrasound in acetone, followed by another 10 minutes in isopropyl alcohol, rinsing with water, an additional 10 minutes on a hot plate at 120 ºC, and finally drying with a N_2 gun.

To study the TiN and AZO film's conformality, PEALD and ALD depositions were performed using substrates composed of a trench patterned polyimide coating (HD Microsystems P2610) on glass (A.4), in the

Picosun system[1]. The polyimide/glass substrates were deposited by spin coating and cured at 350 ºC. The trenches were created on the polyimide surface, by firstly, coating the polyimide/glass with aluminium, followed by photoresist, exposing the photoresist with direct laser writing using a *Heidelberg μPG 101 Tabletop Micro Pattern Generator*, developing it using AZ 726 metal ion free (MIF) developer, then dry-etching the aluminium exposed areas and the polyimide beneath it, exposing the glass substrate, on selected square parts, forming arrays of trenches with dimensions ranging from 3 μm to 22 μm in length/width and 1.9 μm deep.

Table 4: Thermal ALD deposition conditions for the AZO thin films.

AZO Sample	**150-59:1**	**150-69:1**	**150-79:1**	**150-99:1**	**150-129:1**	**180-59:1**	**180-69:1**	**180-79:1**	**180-99:1**	**180-129:1**
T (˚C)	150					180				
DEZ:TMA	59:1	69:1	79:1	99:1	129:1	59:1	69:1	79:1	99:1	129:1
Num. cycles	420		400		390	420		400		390

2.2 Thin Film Characterization

The AZO thickness was obtained using a *DektakXT Bruker* profilometer after etching part of the samples with an aqueous solution of 10% HCl. Afterwards, a *Zeiss Auriga CrossBeam Workstation* SEM-FIB system was used to measure the thickness of an AZO sample. Conversely, the TiN thickness was obtained from TEM images using a *Jeol JEM 2100* electron microscope.

Chemical composition analysis was obtained from X-ray photoelectron spectroscopy (XPS) measurements using a *Kratos Axis Supra system*, with a monochromatic Al Kα radiation source, an X-ray power of 150 W, and pass energy 160 eV for the wide scans, and 20 eV for the detailed scans. The samples were submitted to a cleaning process of Argon ion (Ar^+) sputtering of 5 keV, for several passes of 1 or 2 minutes each, to get the depth profile composition. X-ray diffraction (XRD) measurements, with a *PANalytical's X'Pert PRO MRD system*, with a Cu Kα (wavelength 1.540598 Å) X-ray source provided insight into the crystallinity of the thin films. Additionally, Raman Spectroscopy, with a *Renishaw Qontor Raman Microscope system,* was used with a 532 nm laser at 50 W (10 passes of 10 s each). Scanning electron microscopy (SEM), with a *Hitachi Regulus 8220 system,* was employed to acquire EDS measurements of the AZO samples, to detect the aluminium content (%Al).

A *Tescan Solaris Ga* FIB-SEM system was employed to determine film thickness and to study conformality of AZO and TiN growth on PI/glass substrates.

For the TiN electrical measurements, a *Lake Shore Cryotronics 8400 series Hall measurement system* was used to perform measurements in the van der Pauw configuration, with sample supports already containing gold coated contacts, while for the AZO, contacts of 100 nm of Al needed to be deposited by E-beam evaporation, in a home-made tool. In this case, a *Nanometrics HL5500 Hall effect system* was used.

Post-treatments included UV-Ozone (at room temperature) and Rapid Thermal Annealing (RTA), which were performed using a *Novascan PSD-UV* system and a *AnnealSys One 100 Rapid Thermal Processing* system, respectively.

[1] For the conformality study the *Picosun* reactor at Tyndall was used to deposit both TiN and AZO films due to a damaged component of the *Beneq* reactor that was only possible to replace at a very late stage of this work.

3. RESULTS AND DISCUSSION

3.1 TiN Film Growth

The thickness of the TiN samples was obtained using TEM images of one sample as a reference (Figure 6), in conjunction with the %Ti decay, and %Al rise, from the TiN/Al_2O_3 interface, with the Ar^+ sputtering time (Figure 7), obtained from XPS depth profiles of a few selected samples. By knowing the thickness of sample 300H20b-Capped (39.4 ± 0.4 nm from Figure 6), the thickness of the remaining samples was extrapolated using the average between the thicknesses obtained from the sputter times corresponding to the %Ti and %Al half maximum values (A.5) [25].

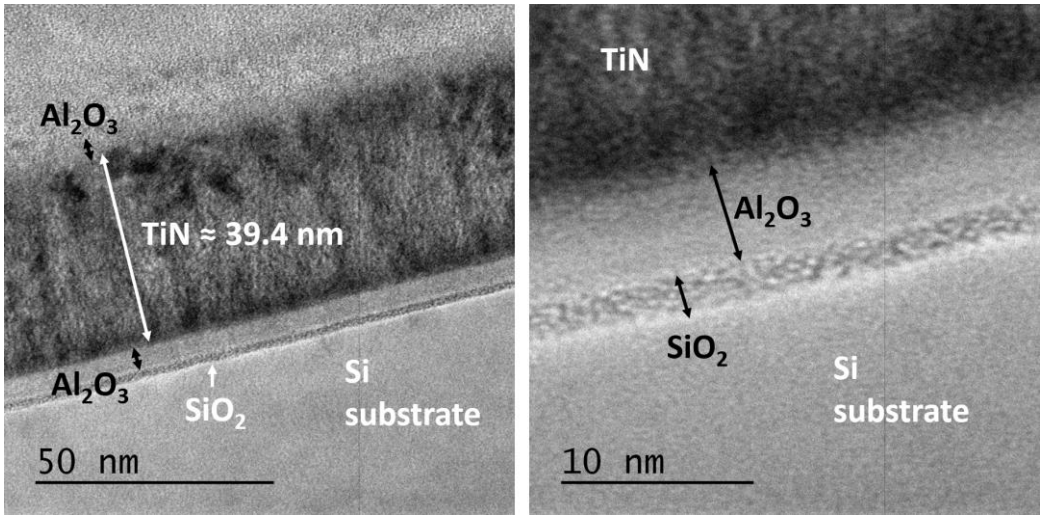

Figure 6: Brightfield TEM images of TiN sample 300H20b-Capped, with identification of the layers and their thickness from surface to substrate: Al_2O_3 capping with 3.6 ± 0.6 nm, TiN with 39.4 ± 0.4 nm, Al_2O_3 with 4.8 ± 0.1 nm and SiO_2 with 1.8 ± 0.1 nm.

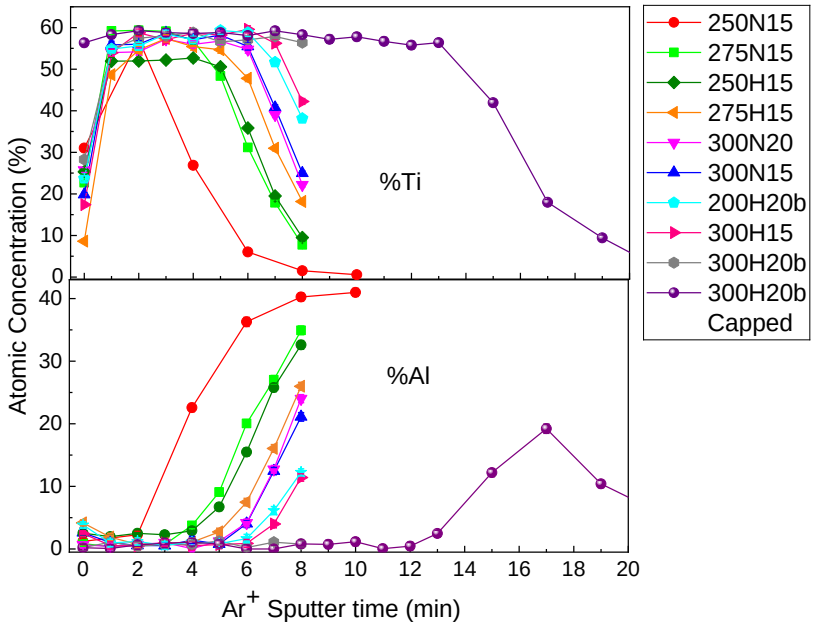

Figure 7: XPS %Ti and %Al depth profile of selected TiN samples.

Table 5: Thickness of TiN samples measured with XPS depth profiles.

Sample	t (nm)
250N15	10.6 ± 0.9
275N15	16.3 ± 1.6
250H15	17.4 ± 1.2
275H15	19.6 ± 2.5
300N15	20.8 ± 2.3
300N20	21.1 ± 2.6
200H20b	21.2 ± 1.5
300H15	24.2 ± 2.9
300H20b-Capped	39.4 ± 0.4

Ellipsometry could not be used to measure the TiN thickness because of the complexity of both the film composition and the layers in the samples that did not allow a reasonable fitting with existing models. Additionally, dry etching part of the films did not produce quality results due to concurrent etching of the substrate, so the TEM image and the XPS depth profiles were the only acquired data allowing thickness estimation.

For each set of equal conditions of precursor pulse, plasma composition, and duration, the thickness seems to increase with temperature which implies that the process is outside (more precisely above) the ALD window, most likely due to thermal decomposition of the TDMAT [5], causing a temperature dependent CVD-like growth, as can be seen by the increase of GPC with increasing temperature (Figure 9). Accordingly, some authors have not observed an ALD window, because of the low temperature onset of TDMAT thermal decomposition [9,26]. In terms of plasma composition, the N_2 plasma samples are thinner than the ones obtained using H_2/N_2 plasma, which can be due to a higher reactivity of NH· radicals compared to N· radicals, causing enhanced deposition rates [7].

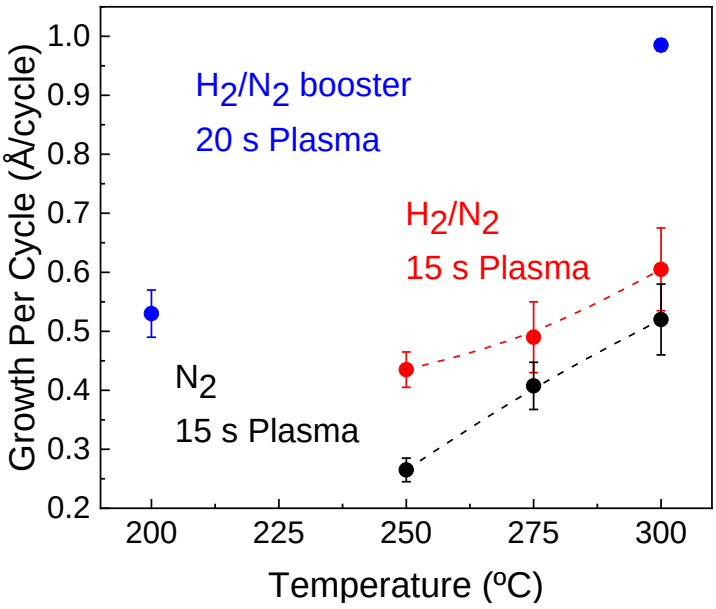

Figure 8: Growth per Cycle of TiN samples using 15 s of N_2 plasma, 15 s of H_2/N_2 plasma and 20 s of H_2/N_2 plasma with the "booster" condition.

As expected, the plasma pulse duration does not have a significant impact on the thickness [26], as can be seen by the proximity of the fitting lines of both the %Ti and the %Al, and consequently, similar thickness of samples 300N15 and 300N20.

The impact of the precursor pulse duration and booster use on thickness is very high, as verified by the thickness of 200H20b (temperature of 200 ºC) being greater than samples deposited at higher temperatures (250H15 and 275H15), and the 300H20b-Capped being the thickest sample by far, which indicates there could be greater TDMAT incorporation in films using the 2 s and booster condition, and that this effect increases notably with temperature [9].

Compared with similar reported literature GPC values, the growth obtained in this work was inferior to the growth of processes using similar temperatures (Table 1), which points to a possible nucleation delay occurring in this case.

Regarding the Al_2O_3 growth, it can be calculated from Figure 6 that this material shows a higher GPC when the substrate is TiN (1.8 Å/cycle), compared with its GPC for a silicon substrate (1.0 Å/cycle). This could be due to an enhanced affinity of the TMA for the TiN surface groups, compared with a possible nucleation delay occurring on the silicon surface [2].

3.2 TiN Structure and Composition

3.2.1 X-ray Photoelectron Spectroscopy

XPS measurements of the TiN samples provided insight into the atomic concentrations of the different elements present in the deposited layers. A few samples were selected to compare different conditions and examine their composition, by measuring all elements present in the wide scans as well as the different bond states of the Ti 2p, N 1s, and C 1s detailed scans. The samples selected are displayed in Table 6, and include different temperatures, plasma gas compositions and durations, as well as distinct precursor pulse durations. Finally, the effect of depositing a capping layer of 20 cycles of Al_2O_3 on the 300H20b sample was included in the XPS results to compare with the original sample (300H20b), which had been exposed to air.

Table 6: XPS average atomic concentration of Ti, N, O, C, and other elements obtained from the depth profiles.

Atomic %	250N 15	275N 15	300N 15	300N 20	250H 15	275H 15	300H 15	200H 20b	300H 20b	300H20b-Capped
Ti	57.2 ± 0.9	59.2 ± 0.9	57.2 ± 0.9	55.6 ± 0.9	52.2 ± 0.8	55.8 ± 0.9	57.7 ± 0.9	57.0 ± 0.9	57.5 ± 0.9	57.7 ± 0.9
N	20.3 ± 0.6	20.5 ± 0.6	19.8 ± 0.6	18.2 ± 0.5	18.4 ± 0.6	15.7 ± 0.5	18.6 ± 0.6	17.5 ± 0.6	17.5 ± 0.6	20.5 ± 0.6
O	15.5 ± 0.8	12.2 ± 0.8	13.0 ± 0.8	20.5 ± 0.8	20.6 ± 0.7	22.9 ± 0.7	16.9 ± 0.8	18.4 ± 0.8	15.5 ± 0.8	14.3 ± 0.8
C	3.6 ± 0.7	6.3 ± 0.7	5.5 ± 0.7	1.5 ± 0.6	4.7 ± 0.7	1.8 ± 0.7	3.3 ± 0.7	4.8 ± 0.7	7.1 ± 0.7	3.0 ± 0.7
Others	3.4 ± 0.5	1.8 ± 0.5	4.6 ± 0.5	4.2 ± 0.5	4.2 ± 0.4	3.8 ± 0.5	3.6 ± 0.5	2.3 ± 0.4	2.4 ± 0.5	4.5 ± 0.5

The depth profile of sample 300H20b-Capped (Figure 9) clearly proves the presence of the deposited layers by the change of the elemental concentrations with the Ar^+ sputtering time, which translates into depth of the sample. From the depth profiles, the atomic concentrations of the present elements were obtained (Table 6) by calculating the average of the flat part, which physically corresponded to the TiN layer.

It should be noted that argon is known to cause preferential sputtering of lighter elements, like oxygen and nitrogen, which can lead to sub-stoichiometric TiN [27]. Nevertheless, in relative terms, these measurements can still be compared as the samples have similar composition, and this is the usual method used to measure the atomic concentration of TiN samples ex-situ [5,7].

Results show that the TiN samples contain high levels of oxygen and considerable carbon contamination, which is expected to happen with ALD of metalorganic precursors [4], meaning that the TiN films are actually composed of TiN_xO_y. Zinc impurities were also detected in every sample, these are thought to come directly from the reactor due to other processes using DEZ precursor. The oxygen is thought to come from the atmosphere, and also from the H_2O pulses during the Al_2O_3 deposition which can easily be incorporated into the film, as Ti reacts spontaneously with water [6], either occupying nitrogen vacancies or even substituting nitrogen and forming Ti-O bonds [5]. Therefore an oxide layer is formed at the surface, evolving to an

oxynitride in the bulk [6]. This can be observed in the rising levels of oxygen closer to both Al_2O_3 layers encapsulating the TiN sample (Figure 8).

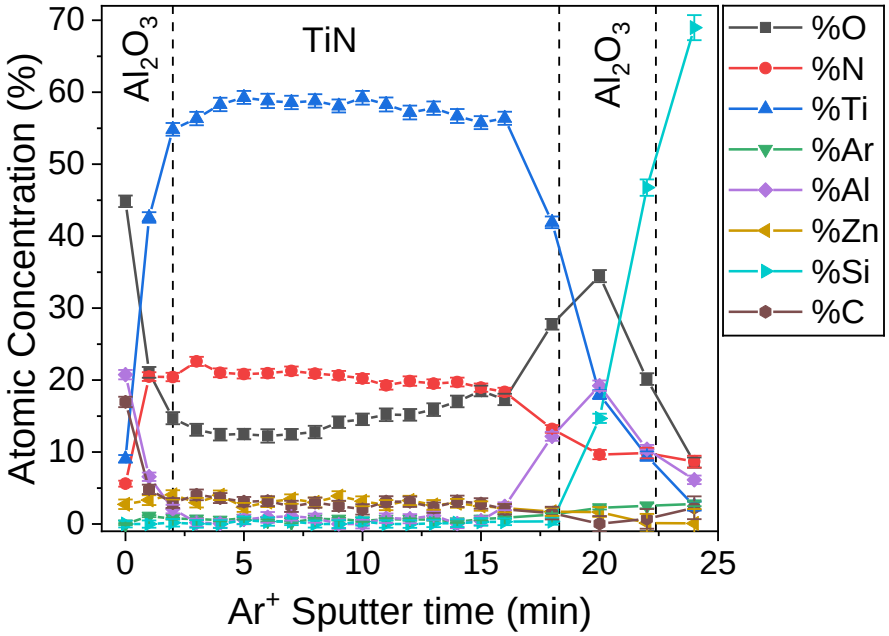

Figure 9: XPS elemental depth profile of the TiN sample 300H20b-Capped as a function of Ar^+ sputter time.

In the detailed scan of the Ti 2p orbital (Figure 10 and Figure 40) three different duplet peaks can be identified: the Ti 2p 3/2 peak around the binding energy of 455 eV corresponds to the Ti-N bonds, the peak around 456 eV is from the Ti-N-O bonds, and the peak around 458 eV is attributed to the Ti-O bonds [6]. To identify these peaks a model was created from literature values and was fitted to every measurement, using peak area, FWHM, and energy restrictions, as described in appendix A.6. As mentioned by J. Musschoot et al. [26], the energy from the Ti-C bond is very close to the Ti-N energy, so it is easier to identify this bond in the C 1s peak. In the C 1s peak at the native surface, there are many C-H and C-O bonds, yet after just 60 s of Ar^+ sputtering the C-Ti peak is visible at the binding energy of 282 eV, with the remaining hydrocarbon C-H bonds agglomerating around the binding energy of 285 eV (Figure 41, A.6) [4].

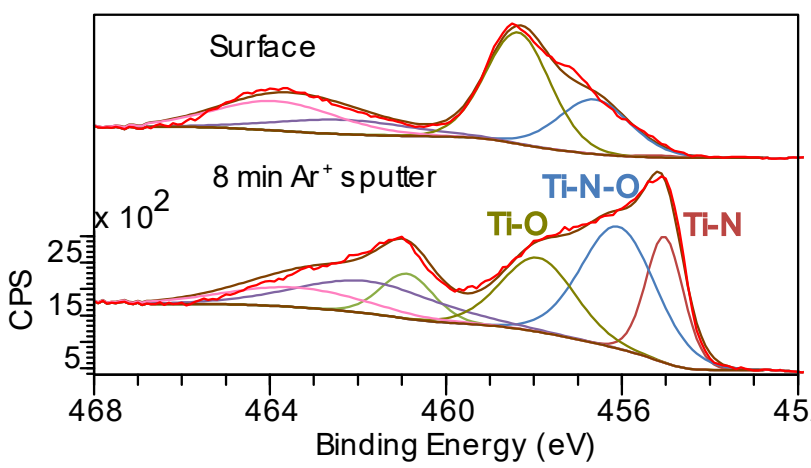

Name	Pos.	FWHM	%Area
Ti 2p3/2 Ti-N	455.21	1.00	0.68
Ti 2p1/2 Ti-N	461.06	1.40	0.00
Ti 2p3/2 Ti-N-O	456.62	1.91	35.14
Ti 2p1/2 Ti-N-O	462.32	3.62	0.00
Ti 2p3/2 Ti-O	458.36	1.71	64.18
Ti 2p1/2 Ti-O	463.86	3.24	0.00

Name	Pos.	FWHM	%Area
Ti 2p3/2 Ti-N	455.03	1.01	24.98
Ti 2p1/2 Ti-N	460.88	1.41	0.00
Ti 2p3/2 Ti-N-O	456.09	1.98	46.52
Ti 2p1/2 Ti-N-O	461.79	3.75	0.00
Ti 2p3/2 Ti-O	457.91	1.97	28.50
Ti 2p1/2 Ti-O	463.41	3.75	0.00

Figure 10: XPS detailed scan of Ti 2p peak at the surface of the 300H20b sample and after 8 minutes of Ar^+ sputtering. Includes fitting of the components Ti-N, Ti-N-O, and Ti-O, forming the envelope in brown, and raw data in red.

The difference in oxidation from the native surface to the bulk of the films is also clear in Figure 10, showing the Ti 2p peak with a higher oxide component (Ti-O) on the surface of sample 300H20b, which decreases in the bulk, as opposed to the nitride (Ti-N) component, and an intermediate oxynitride component (Ti-N-O), that is always present. This oxidation gradient is also visible in the N 1s spectrum (Figure 11), which has higher oxidized components (%N-Ti-O at 396.3 eV and N-O-Ti at 399.5 eV [28]) on the surface, and a higher nitride component (%N-Ti at 397.1 eV) in the bulk of the film.

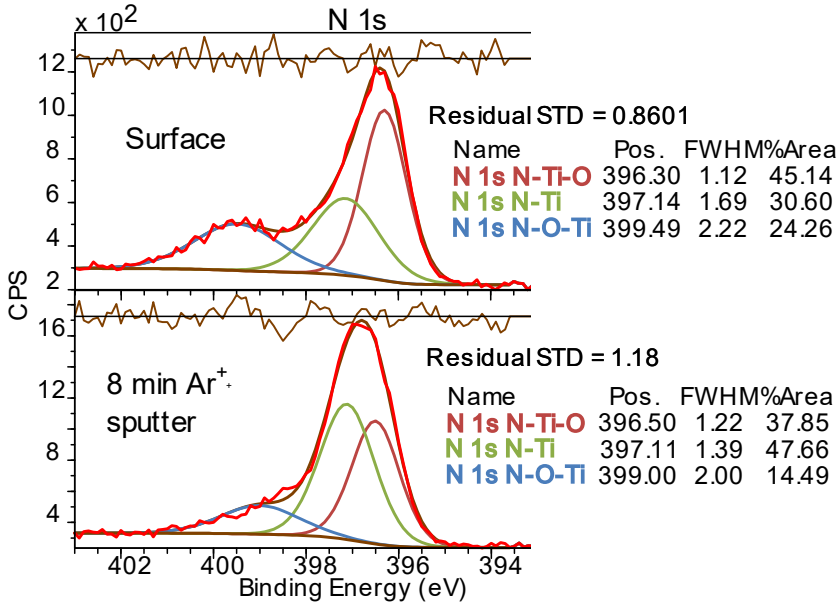

Figure 11: XPS N1s peak from the TiN sample 300H20b native surface and after 8 minutes of Ar^+ ion sputtering.

It is possible to use the Ti 2p and C 1s components to calculate percentages of each component within those peaks (Table 7), and compare different samples in terms of bond types, by accessing their level of bulk oxidation and hydrocarbon contamination, which are tightly related to their resistivities [10].

Table 7: XPS Ti 2p and C 1s peak components model fitting results calculated with *casaxps*.

Atomic %	250N 15	275N 15	300N 15	300N 20	250H 15	275H 15	300H 15	200H 20b	300H 20b	300H20b -Capped
Ti-N	24.5 ± 0.8	26.4 ± 0.8	24.9 ± 0.8	20.4 ± 0.8	20.6 ± 0.8	22.8 ± 0.8	22.4 ± 0.8	22.0 ± 0.8	23.9 ± 0.8	26.9 ± 0.8
Ti-N-O	46.6 ± 0.8	46.9 ± 0.8	46.8 ± 0.8	37.5 ± 0.8	41.4 ± 0.8	35.2 ± 0.8	42.1 ± 0.8	44.0 ± 0.8	47.2 ± 0.8	45.8 ± 0.8
Ti-O	28.9 ± 0.8	26.7 ± 0.8	28.3 ± 0.8	42.2 ± 0.8	38.0 ± 0.8	42.0 ± 0.8	35.4 ± 0.8	33.9 ± 0.8	28.9 ± 0.8	27.3 ± 0.8
C- Ti	62.6 ± 13.8	56.0 ± 9.3	52.8 ± 8.0	60.3 ± 25.5	51.0 ± 10.2	63.4 ± 26.7	61.2 ± 15.3	54.0 ± 9.5	49.2 ± 7.3	63.1 ± 12.4
C-H	37.4 ± 13.8	44.0 ± 9.3	47.2 ± 8.0	39.7 ± 25.5	49.0 ± 10.2	36.7 ± 26.7	38.8 ± 15.3	46.0 ± 9.5	50.8 ± 7.3	36.9 ± 12.4

The Al_2O_3 capping layer on sample 300H20b-Capped allowed less oxygen (%O) introduction (Table 6), compared with the uncapped sample (300H20b). This reinforces the idea that oxygen is partly incorporated ex-situ, and is probably substituting nitrogen in the film, as the capped sample also shows a 2.9% higher nitrogen. Considering that the uncapped sample was not etched all the way through, and that the capped sample's first depth profile points get information from the Al_2O_3, it is still possible to see that the %Ti-N is higher, and the %Ti-O is lower for the capped sample in the first nm, while these levels seem to equalize afterward (Figure 12). It also shows 4.1% less total carbon and 13.9% less %C-H (Table 7), meaning that carbon impurities from the atmosphere (hydrocarbons C-H) may be introduced in the film post-deposition.

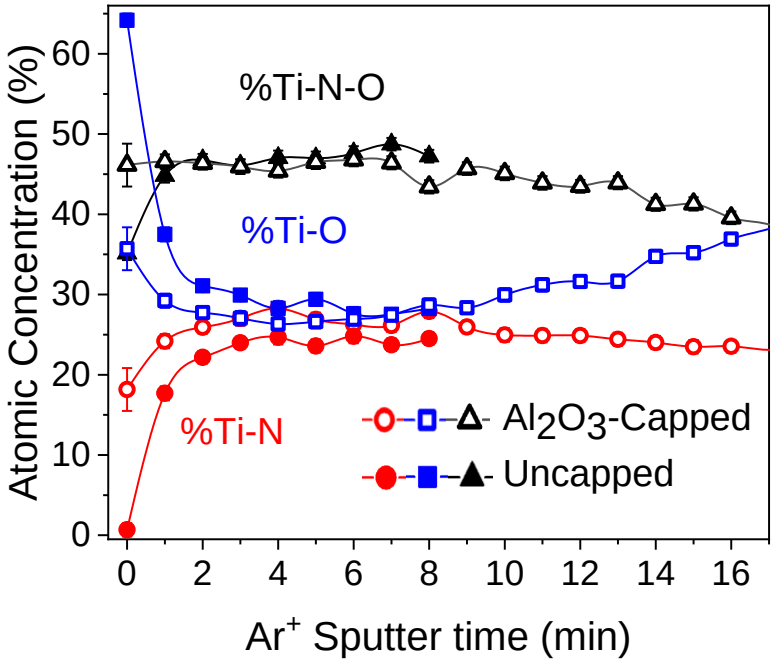

Figure 12: XPS atomic concentration of the Ti 2p components: Ti-N, Ti-N-O, and Ti-O for the 300H20b Al_2O_3 capped and uncapped samples.

Overall, capping the sample with only 20 cycles of Al_2O_3 was not very effective in preventing bulk oxidation of the Ti, because this Al_2O_3 layer is only 3.6 nm thick, moreover, it uses H_2O pulses which easily react with the Ti to form Ti-O bonds, and this presumably happens because the TiN samples are very porous, and impure [9].

3.2.2 X-ray Diffraction

XRD measurements show the crystallinity of selected TiN samples with distinct plasma composition and duration (Figure 13 a)), temperature (Figure 13 b)), and number of cycles (Figure 14). All these films are weakly crystalline, which is expected from PEALD using metalorganic precursors, due to carbon and oxygen impurities [9]. N_2 plasma samples have a preferential (200) orientation [5], and their crystallinity increases with plasma duration, as the film surface receives more energy [10], with sample 300N20 presenting the most defined peak with TiO (200) orientation, coinciding with its high oxygen concentration (Table 6). While in the case of the H_2/N_2 plasma the preferential orientation is changing from (200) to (111) with the plasma time, which could be due to a dominant effect from the hydrogen in the H_2/N_2 that only occurs above 15 s plasma.

When it comes to temperature, the crystallinity does not change significantly for the H_2/N_2 "booster" samples (Figure 13 b)), possibly due to the high levels of carbon in these samples, which also increase with temperature, counterbalancing the natural tendency of crystallinity to increase with temperature [29].

The crystallinity increases with the number of cycles (Figure 14), as the samples get thicker and can form larger grains. Nonetheless, all the XRD peaks are very broad and weak, even for the thickest sample (300H20b-1500), and include TiC, TiN and TiO reference values [6,30], corroborating the high level of carbon and oxygen impurities in the films, which appear to have a significant impact on their structure.

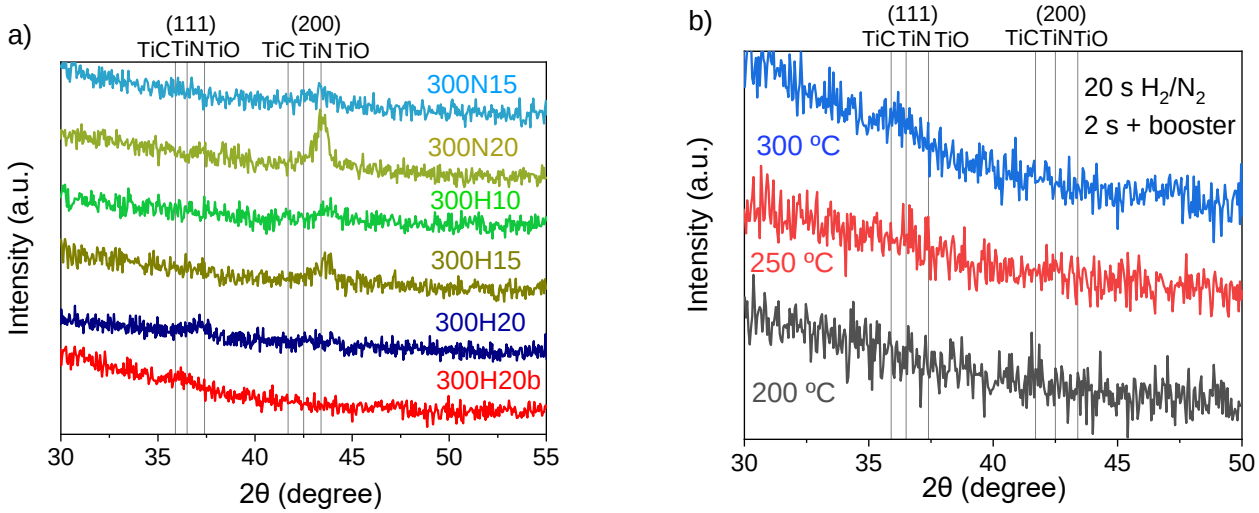

Figure 13: XRD results of samples with a) different plasma composition and duration and b) different deposition temperatures: 300 ºC, 250 ºC and 200 ºC, with identification of reference peaks of TiC (111) at 35.9º, TiN (111) at 36.5º, TiO (111) at 37.4º, TiC (200) at 41.7º, TiN (200) at 42.5º and TiO (200) at 43.4º [6,30].

Raman Spectroscopy measurements provided a spectrum of sample 300H20b-1500 (Figure 16), showing the intrinsic acoustic and optical transitions of TiN: transverse acoustic (TA) at around 250 cm^{-1}, longitudinal acoustic (LA) at 320 cm^{-1} [31], and transverse optical (TO) at 580 cm^{-1} [32], besides the strong signal of the Si-Si peak from the substrate at 520 cm^{-1}, which masked any signal detection of the thinner samples.

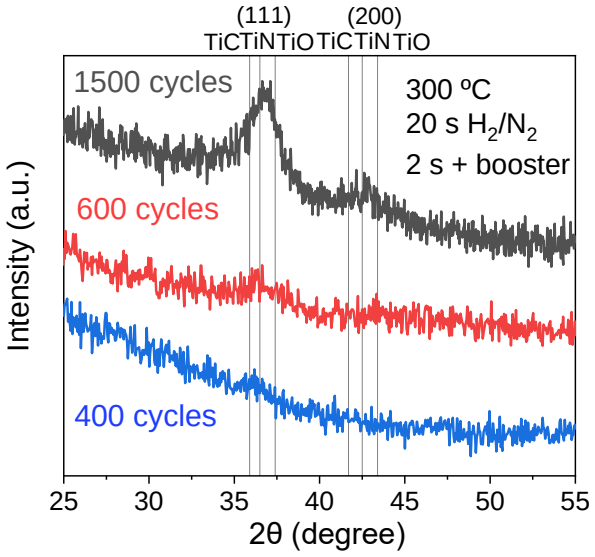

Figure 14: XRD spectra of samples with different deposition number of cycles.

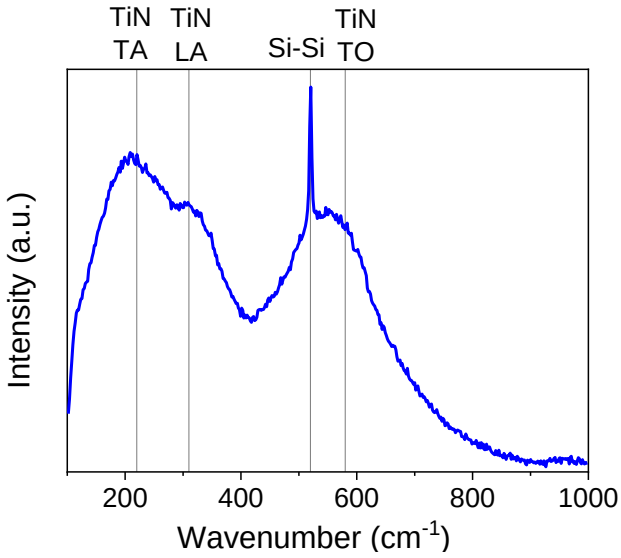

Figure 15: Raman spectrum of sample 300H20b-1500.

3.3 TiN Electrical Properties

The effects of deposition temperature and plasma pulse duration on the resistivity are depicted in Figure 16 a) and b). As typically occurs in the literature, the resistivity decreased with increasing temperature, which can be explained by the higher density of thin films grown with superior temperatures, and also, a larger thickness which decreases the sheet resistance, by reducing electron scattering phenomena [5]. The resistivity of sample 250N15 could not be measured, due to a lack of uniformity of the film, which led to the adoption of the longer precursor pulse time, with the assistance of a booster of 600 sccm of N_2. This change in the process conditions produced a more resistive sample (300H20b), compared to the original sample using the same remaining conditions (300H20). This is explained by the use of a longer precursor pulse which allowed more TDMAT thermal decomposition and its subsequent incorporation in the film in the form of C-H bonds, which is also the most probable cause for a 15 nm superior thickness, forming a porous and unstable film structure that would allow oxygen incorporation [5,6].

In terms of temperature, the H_2/N_2 booster samples show both a thickness trend and a difference in composition, namely oxygen contamination, that explains why 300H20b is 56.4% more conductive than 200H20b. Indeed, besides being thicker, sample 300H20b has 2.9 % less oxygen, 1.9% higher %Ti-N, 3.2 % more %Ti-N-O and 5% lower %Ti-O. Despite having 2.3% higher carbon and 4.8% more %C-H (due to an increased precursor decomposition for 300 ºC deposition temperature [5]), the evident contrast of thickness and oxygen levels are the factors that influence the most the resistance.

Additionally, the resistivity also decreased with the plasma pulse duration for the H_2/N_2, as expected [8], while for the N_2 plasma it decreased until 15 s, but increased for the 20 s sample (Figure 16 b)), which can happen due to higher oxygen contamination in high-pressure processes [5], as the one used in the present work (reactor pressure of 4.5 Torr). In fact, from the XPS results of samples 300N15 and 300N20, there is 7% more oxygen incorporation for the longer plasma condition (Table 6). This sample also has 13.9% more %Ti-O, 9.3% less %Ti-N-O, and 4.5% less %Ti-N (Table 7), compared with the 15 s plasma sample.

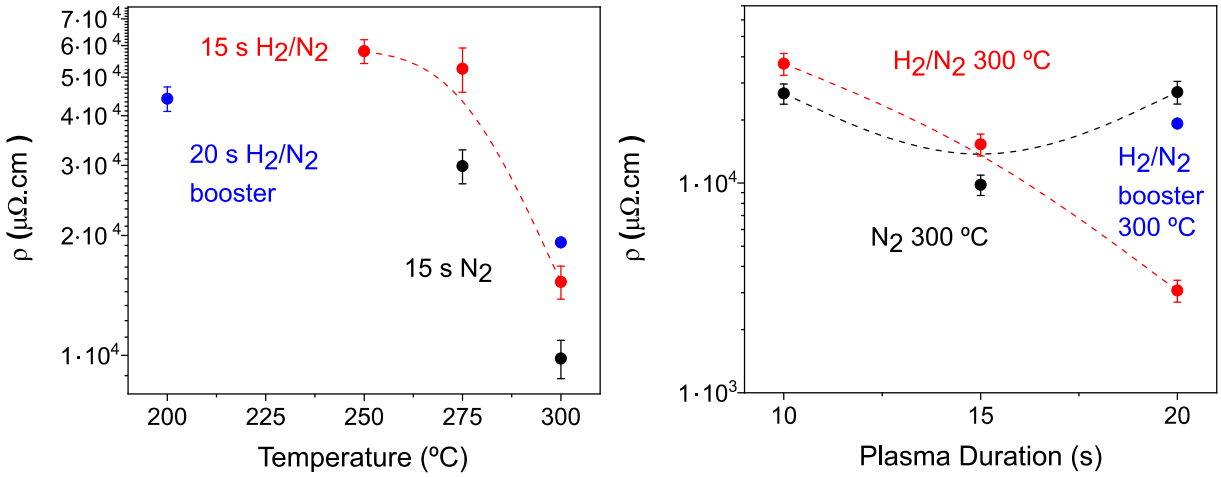

Figure 16: TiN resistivity as a function of a) deposition temperature and b) plasma duration.

For different plasma composition, among the samples deposited with 15 s of plasma pulses, the lowest resistivity was attributed to the N_2 plasma (Figure 16 a)), which can also be explained by the lower level of oxygen, 10% less for the 275 ºC, and 3.9% less for the 300 ºC N_2 plasma samples compared with their H_2/N_2 counterparts. Even though the N_2 plasma samples have more carbon and are thinner, as I. Krylov et al. [5] states, more C-Ti bonds can avoid oxygen intake by the film by forming a conductive carbide phase [29]. Again, the oxygen concentration is the factor influencing the most the resistivity.

The analysis of the effects of temperature and plasma duration against one another for H_2/N_2 plasma samples shows that extending the plasma duration from 10 s to 20 s causes a 91.7% reduction in resistivity, while increasing the temperature from 250 ºC to 300 ºC reduces it by 73.7%. Therefore, these particular process conditions indicate that plasma duration has a larger impact on the electrical properties of these TiN films, so longer plasma durations should be investigated.

Moreover, the resistivity shows a decreasing trend with the number of cycles due to an increase in thickness, which, as previously mentioned, reduces the effect of surface scattering and grain boundary scattering. As the crystallinity was slightly enhanced with the number of cycles (Figure 17), it means the grains must be larger for the thicker films, therefore reducing grain boundary scattering, and contributing to higher conductivity [5].

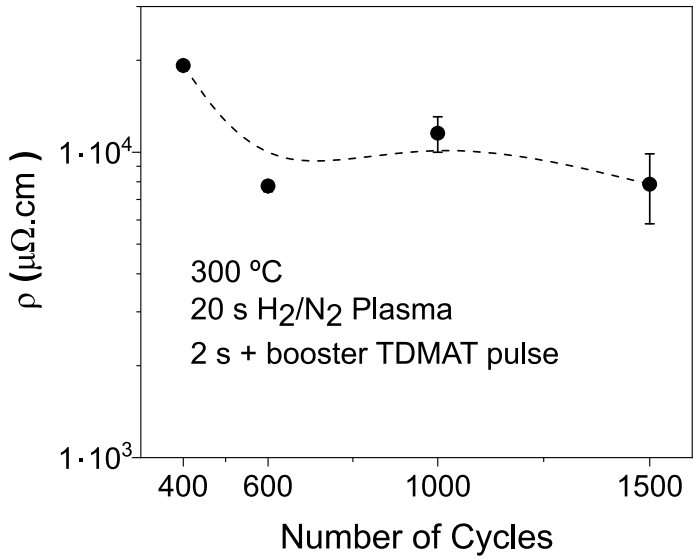

Figure 17: Resistivity of TiN samples as a function of the number of cycles of the PEALD deposition.

In conclusion, the lowest resistivity value was obtained for sample 300H20, and it resulted in 3073.4 μΩ.cm, which is higher than most literature values (Table 1). The reasons behind the high resistivity obtained for all TiN samples have to do with the high level of CVD-like deposition, which led to the incorporation of high amounts of amine groups, forming unstable and resistive C-H bonds in the film, and also due to a long precursor pulse time, especially the 2 s and booster depositions, which allowed the TDMAT to decompose on the growing film's surface. This happened to such a degree because the reactor pressure was too high (4.5 Torr compared with a maximum of 1 Torr, in the presented literature), which decreased the onset decomposition temperature of the TDMAT [5], increasing the incorporation of this species, and, consequently, inhibiting the formation of Ti-N bonds. This unstable and porous structure led to the oxidation of the films by reaction with oxygen from the air [6], that easily penetrated and bonded to the Ti atoms, replacing nitrogen and filling nitrogen vacancies [5].

3.4 AZO Film Growth

The AZO film thickness was obtained by profilometry, and the results are present in Table 8. By dividing the film thicknesses by each sample's respective deposition number of cycles the GPC was calculated (Figure 18). The GPC of samples deposited at 150 ºC is slightly higher than the ones deposited at 180 ºC (Figure 18). This difference is also observed for undoped ZnO films and can be caused by a decrease of the hydroxyl

group (-OH) surface coverage with increasing temperature, due to water desorption [14]. Another possible cause is that a temperature of 150 ºC does not allow the precursor groups to completely react with the H_2O molecules, what can lead to their incorporation in the film [33].

The variance of GPC for each deposition temperature, as a function of DEZ:TMA ratio, can be influenced by an effect described as etching of TMA on ZnO surfaces [20], where the TMA/H_2O cycle can reduce the growth rate of the following ZnO/H_2O cycles (up to negative values), until it recovers its usual bulk growth value. In theory, this phenomenon continuously decreases the GPC with the aluminium content (for lower DEZ:TMA ratios), as was obtained in this case (Figure 18).

Table 8: Profilometry thickness of AZO samples.

T (ºC)	DEZ:TMA	t (nm)
150	59:1	67.8 ± 0.5
	69:1	67.9 ± 1.6
	79:1	64.9 ± 0.7
	99:1	66.6 ± 0.9
	129:1	66.1 ± 1.6
180	59:1	63.9 ± 0.6
	69:1	62.9 ± 1.0
	79:1	61.9 ± 0.2
	99:1	64.9 ± 1.5
	129:1	65.5 ± 0.9

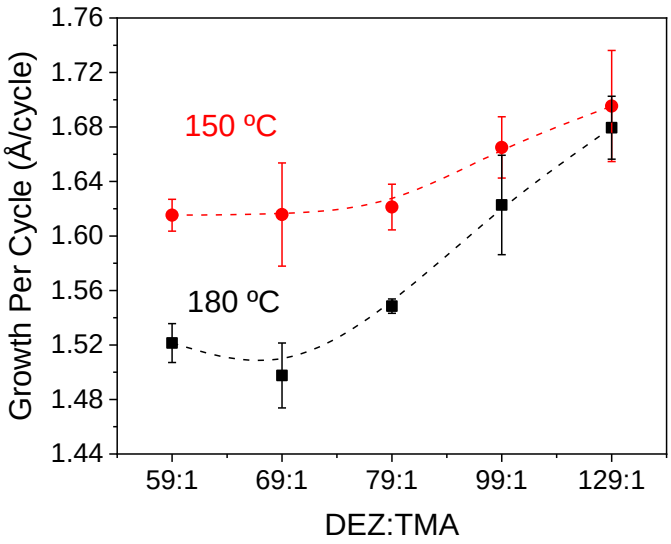

Figure 18: Effect of deposition temperature and DEZ:TMA cycle ratio on the Growth Per Cycle of AZO samples.

Given the opportunity, FIB was used to mill a hole on sample AZO180-59:1, creating a cross-section that was observed by SEM (A.7). This SEM image shows a thickness of approximately 43.5 nm, which is significantly lower than the value obtained by profilometry (63.9 nm).

3.5 AZO Structure and Composition

3.5.1 Energy Dispersive Spectroscopy

EDS measurements provided the elemental concentration of Zn, O, and Al in the AZO samples, of which the %Al is presented in Figure 20. The results obtained with this technique are not very exact, since this method used an incident energy of 15 keV, which penetrated microns into the substrate, interacting and receiving most elemental information from the silicon substrate, as can be seen by the difference in peak intensity between the Si and the elements present in the AZO thin film (Zn, O and Al) (Figure 19). Besides, the Si and Al peaks are very close in energy, 1.739 keV and 1.486 keV respectively, which further affects the results. Even though the differences are very slim, Figure 20 shows more %Al in the films deposited with higher temperatures, which is related to a greater efficacy of the chemical reactions during the film deposition, that can allow higher incorporation of the Al dopant atoms in the ZnO structure [33].

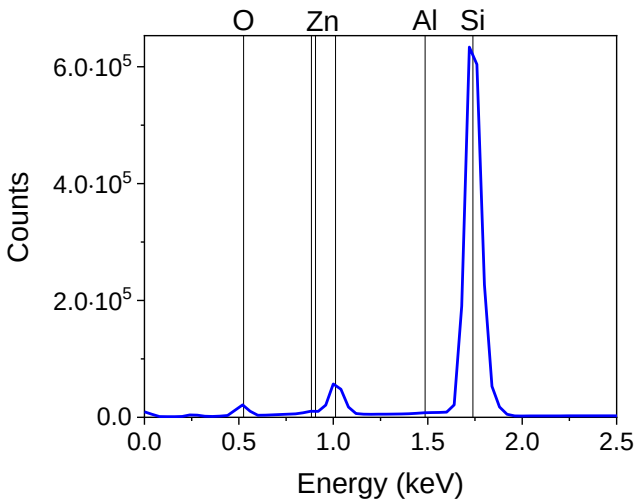

Figure 19: EDS spectrum of sample AZO180-59:1 with identified element emission energies.

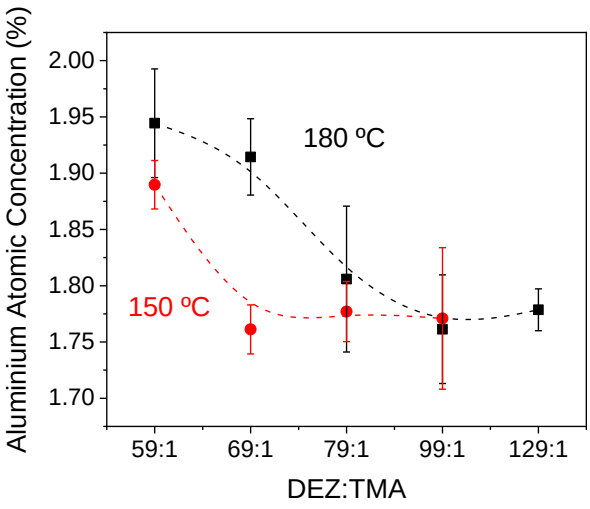

Figure 20: EDS measured Aluminium atomic concentration (%Al) of AZO samples as a function of deposition temperature and DEZ:TMA ratio.

3.5.2 X-ray Diffraction

XRD measurements were performed on two AZO samples with equal DEZ:TMA ratio and different temperatures to observe the effect of temperature on the film crystallinity (Figure 21). Both samples are polycrystalline, presenting the usual planes of ZnO hexagonal wurtzite, identified as (100), (002), (101), (102) and (110), at the diffractions angles of 31.69º, 34.37º, 36.16º, 47.67º and 56.56º [16,19]. All peaks are slightly shifted to larger diffraction angles, which, according to Bragg's law (n.λ=2d.sinθ) means a higher diffraction angle is caused by lower plane distances, in this case, by the Al^{3+} (ionic radius of 0.53 Å) substitution of Zn^{2+} (0.74 Å) [16]. Additionally, this peak shift is similar for both samples, and therefore for both deposition temperatures, which reinforces the proximity of aluminium doping concentration between both films.

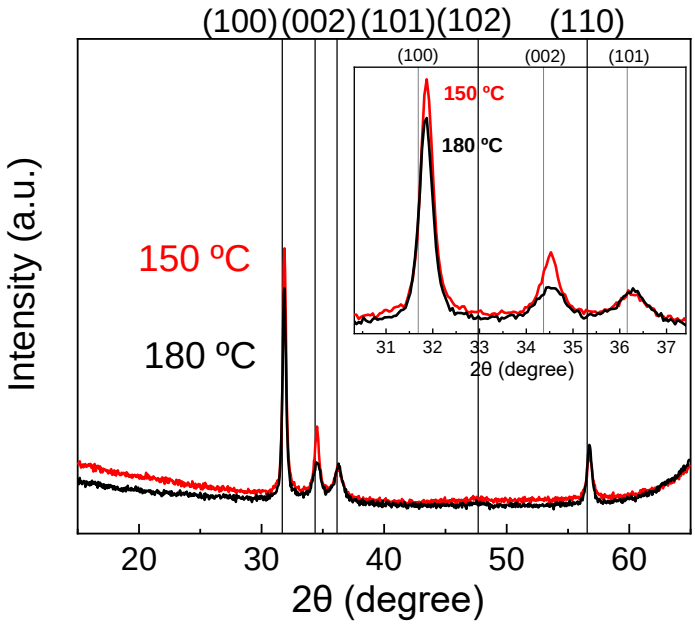

Figure 21: XRD spectra of samples AZO150-59:1 and AZO180-59:1, with inset of peaks (100), (002) and (101).

Notwithstanding that undoped ZnO is usually (002) oriented because of this plane's low surface energy and high atomic density [16], aluminium doping has been shown to supress the formation of the (002) orientation and cause (100) preferential growth [16]. As this effect is observed in the present case, and the (100) is the most intense peak, it was chosen as the object of a more detailed analysis. The (100) crystallite size was calculated using Sherrer's equation ($D=K.\lambda.\beta^{-1}.\cos(\theta)^{-1}$, with K=1 and λ=1.5406 Å). The resulting values show a slightly higher crystallite diameter for the 150 ºC sample (29 nm), compared with the 180 ºC (26 nm), which is not sufficiently clear to conclude on a crystallinity difference between both deposition temperatures.

3.6 AZO Electrical Properties

The electrical properties of the AZO samples, namely resistivity, carrier concentration (N) and mobility (μ), determined from Hall effect measurements, are described in Table 9. Their change with DEZ:TMA ratio and deposition temperature is visible in Figure 22 to Figure 25.

As expected, every sample showed n type conductivity, with carrier concentrations above 10^{20} cm^{-3}, meaning the films can be considered degenerate or close-to-degenerate semiconductors. Consequently, the mobility is not mostly limited by grain barrier scattering, due to electron tunnelling, but is more limited by ionized impurity scattering of electrons [15]. This might explain why the mobilities obtained were low (<11 cm^2/Vs) (Figure 25 b)), but still similar to some of the references [19,21,33].

As the temperature increases from 150 ºC to 180 ºC, the resistivity decreases (Figure 24). Such resistivity behaviour is potentially caused by a more complete removal of precursor ligands during the film deposition at higher temperatures, meaning the films have less impurities, as well as increased aluminium content (Figure 20) [33]. For samples deposited at 150 ºC, the lowest resistivity was obtained for the 69:1 DEZ:TMA ratio (%Al=1.76%) with a value of 4.5×10^{-3} Ω.cm, while for the 180 ºC samples it was the 59:1 ratio (%Al=1.94%) with a value of 2.5×10^{-3} Ω.cm. This suggests that while the DEZ:TMA ratio that minimizes the resistivity may have been reached for the deposition at 150 ºC, it may not have been reached for a deposition temperature of 180 ºC since 1.94% is still below the usual reported %Al, between 1.98% - 3.00% (Table 2). So, to find the ratio that minimizes resistivity lower DEZ:TMA ratios should be investigated.

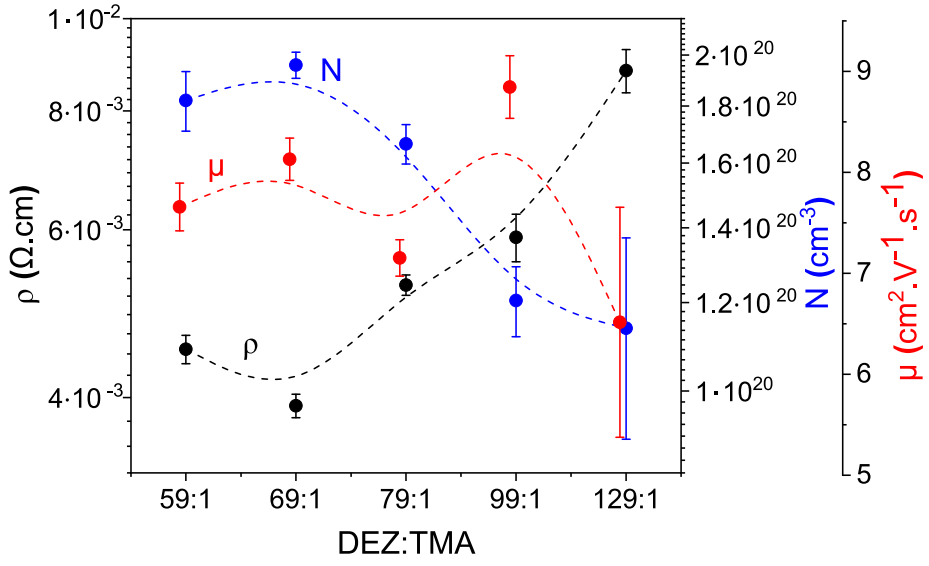

Figure 22: Effect of DEZ:TMA ratio on ρ, μ and N for AZO thin films produced at a temperature of 150ºC.

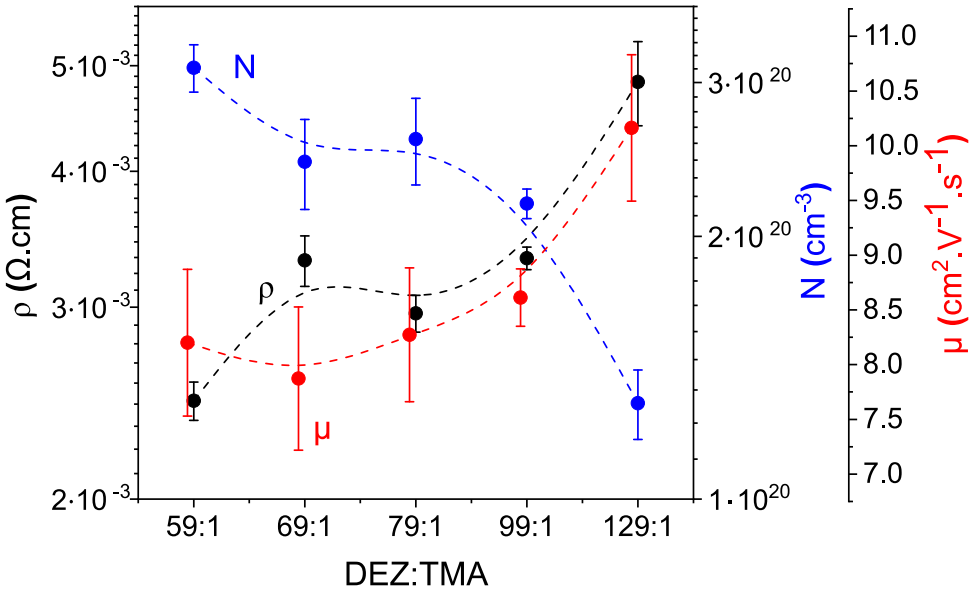

Figure 23: Effect of DEZ:TMA ratio on ρ, μ and N for AZO thin films produced at a temperature of 180ºC.

For each temperature, the resistivity is always inversely related to N (Figure 25 a)) because, as recorded in the literature, ρ decreases continuously with N until saturating at $N=5\times10^{20}$ cm^{-3} [15], a value above the maximum N obtained in this work (3.1×10^{20} cm^{-3}, for AZO180-59:1). Conversely, the mobility's behaviour is hard to describe as the values are all very close, yet there is a tendency for them to be greater for higher temperatures (Figure 25 b)) [16].

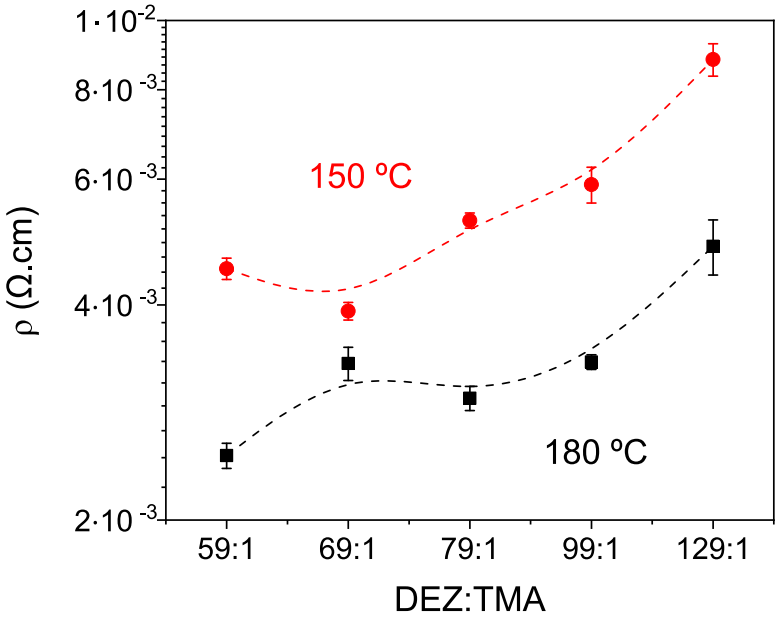

Figure 24: Resistivity (ρ) of AZO samples as a function of DEZ:TMA ratio and temperature.

The resistivity of all AZO was calculated by multiplying the sheet resistance, obtained from the Hall effect measurements, by the thickness obtained with profilometry, however, as previously mentioned, the thickness might, in reality, be inferior, meaning that the resistivity is also lower, and the carrier concentration is higher. Instead of 2.5×10^{-3} Ω.cm and 3.1×10^{20} cm^{-3}, ρ might be as low as 1.67×10^{-3} Ω.cm and N as high as 4.53×10^{20} cm^{-3} for sample AZO180-59:1. Thus, the resistivity obtained for the AZO samples is within the usual ALD AZO literature range (10^{-3} Ω.cm) (Table 4).

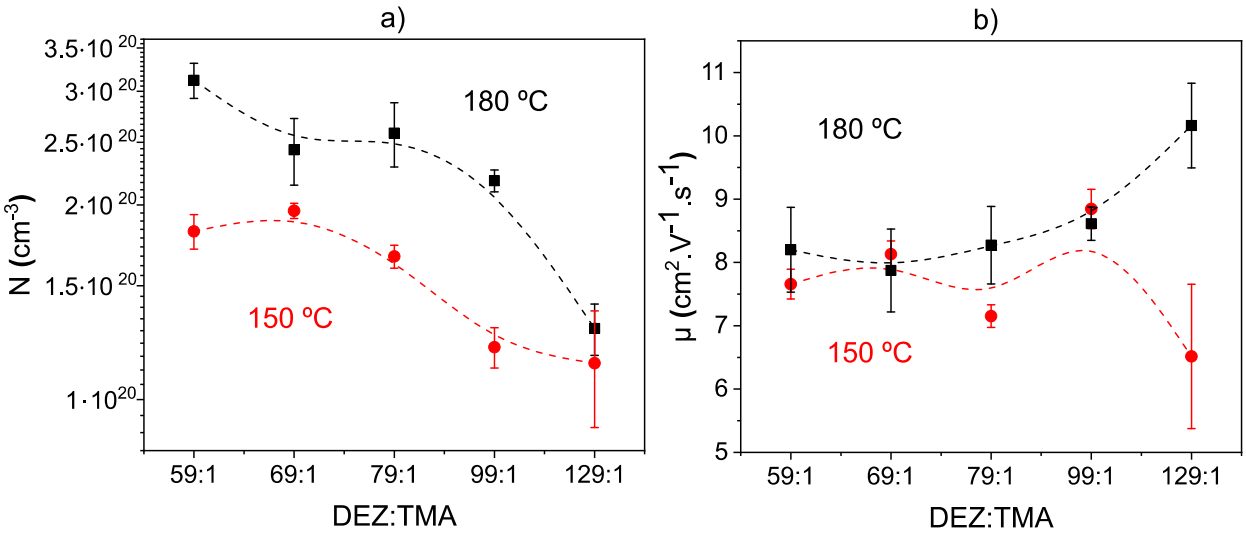

Figure 25: a) Carrier Concentration and b) Mobility of AZO samples as a function of DEZ:TMA ratio and temperature.

Table 9: AZO structural, compositional, and electrical properties.

Sample	DEZ:TMA ratio	Al content (%)	ρ (Ω.cm)	N (cm^{-3})	μ ($cm^2.V^{-1}s^{-1}$)	t (nm)
AZO150-59:1	59:1	1.89 ± 0.02	$4.5\times10^{-3} \pm 1.6\times10^{-4}$	$1.8\times10^{20} \pm 1.1\times10^{19}$	7.7 ± 0.2	67.8 ± 0.5
AZO150-69:1	69:1	1.76 ± 0.02	$3.9\times10^{-3} \pm 1.1\times10^{-4}$	$2.0\times10^{20} \pm 5.3\times10^{18}$	8.1 ± 0.2	67.9 ± 1.6
AZO150-79:1	79:1	1.78 ± 0.03	$5.3\times10^{-3} \pm 1.3\times10^{-4}$	$1.7\times10^{20} \pm 6.8\times10^{18}$	7.2 ± 0.2	64.9 ± 0.7
AZO150-99:1	99:1	1.77 ± 0.06	$5.9\times10^{-3} \pm 3.4\times10^{-4}$	$1.2\times10^{20} \pm 8.7\times10^{18}$	8.9 ± 0.3	66.6 ± 0.9
AZO150-129:1	129:1	-	$8.8\times10^{-3} \pm 4.6\times10^{-4}$	$1.1\times10^{20} \pm 2.3\times10^{19}$	6.5 ± 1.1	66.1 ± 1.6
AZO180-59:1	59:1	1.94 ± 0.05	$2.5\times10^{-3} \pm 1.0\times10^{-4}$	$3.1\times10^{20} \pm 1.9\times10^{19}$	8.2 ± 0.7	63.9 ± 0.6
AZO180-69:1	69:1	1.91 ± 0.03	$3.3\times10^{-3} \pm 1.8\times10^{-4}$	$2.4\times10^{20} \pm 2.9\times10^{19}$	7.9 ± 0.7	62.9 ± 1.0
AZO180-79:1	79:1	1.81 ± 0.06	$3.0\times10^{-3} \pm 1.2\times10^{-4}$	$2.6\times10^{20} \pm 2.9\times10^{19}$	8.3 ± 0.6	61.9 ± 0.2
AZO180-99:1	99:1	1.76 ± 0.05	$3.3\times10^{-3} \pm 7.9\times10^{-5}$	$2.2\times10^{20} \pm 8.5\times10^{18}$	8.6 ± 0.3	64.9 ± 1.5
AZO180-129:1	129:1	1.78 ± 0.02	$4.8\times10^{-3} \pm 4.3\times10^{-4}$	$1.3\times10^{20} \pm 1.2\times10^{19}$	10.2 ± 0.7	65.5 ± 0.9

3.6.1 Post-treatment Study of the AZO samples

To improve the electrical properties of the AZO films, two post-treatment approaches were investigated separately: UV-Ozone (UV-O_3) at room temperature for different durations, and Rapid Thermal Annealing (RTA) at 300 ºC, in N_2 atmosphere for different durations and pressures. Different replicas of the same samples were used to test each condition.

3.6.1.1 UV-Ozone

By submitting replicas of sample AZO180-69 to UV-O_3 treatments of 5, 10, 15 and 30 minutes the resistivity showed a continuous decrease with treatment time up to 30 minutes (Figure 26 a)). More precisely, the resistivity was decreased by 24.8%, to 2.3×10^{-3} Ω.cm for a UV-O_3 treatment with duration of 30 minutes, which is below the lowest as deposited resistivity of the AZO samples (AZO180-59:1) with 2.5×10^{-3} Ω.cm.

The mechanism taking place during an UV-O_3 treatment is a repeated generation cycle of O_3 from exposing O_2 to UV light with λ=184.9 nm, and destruction of O_3 from exposure to UV light with λ=253.7 nm, forming O_2 [34]. The source of O_2 is the ambient air inside the chamber and the film surface [35]. So, during this treatment, O_2 is released from the film by forming O_3. This O_2 removal increases the number of oxygen vacancies in the film, known to enhance the carrier concentration, and reduce resistivity ($\rho=(n.\mu.q)^{-1}$) [36].

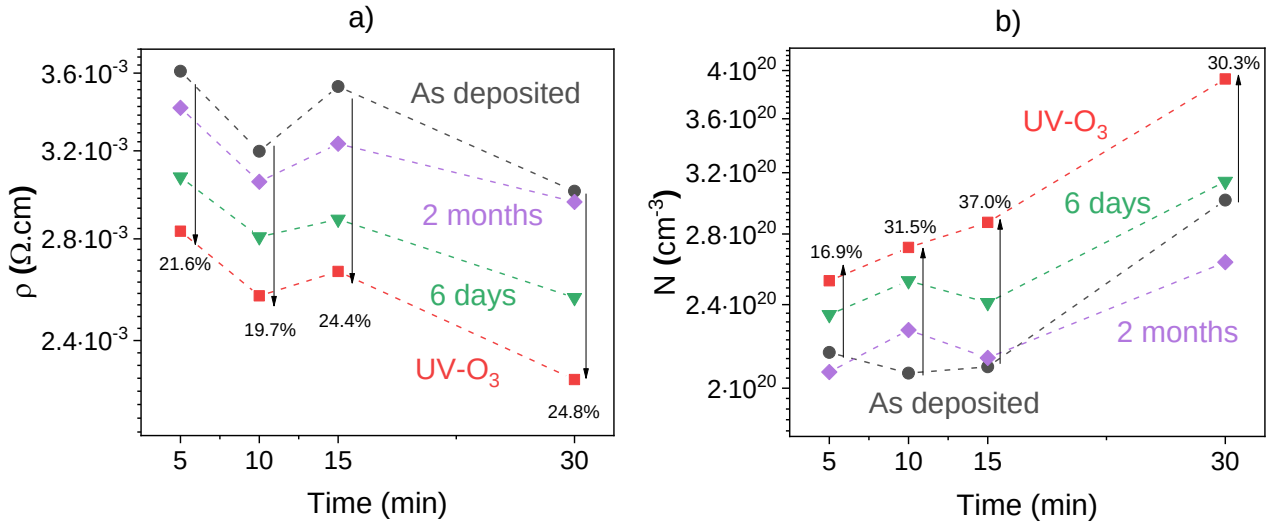

Figure 26: UV-Ozone post-treatments performed on sample AZO180-69:1 for 5, 10, 15 and 30 minutes, with the a) resistivity and b) carrier concentration of measurements after deposition, after UV-O3 treatments, 6 days and 2 months later.

In relative terms, the 15 minutes treatment was the most effective at increasing the carrier concentration, perhaps due to some reincorporation of oxygen into the film for the 30 minutes treatment. Moreover, the mobility is expected to increase due to desorption of oxygen from the grain boundaries (A.8) [35].

An important aspect of this treatment is that its effects are only temporary [35], as can be seen by the increase of resistivity just 6 days after the initial measurement, and a general tendency of resistivity recovery over long periods of time (Figure 26 a)).

To verify the mechanism of oxygen removal from the film and posterior reintroduction with time, another 15 minutes UV-O_3 treatment was performed, this time on two replicas of sample AZO180-129:1. After measuring the electrical properties of UV-O_3 treated samples, one was left at atmospheric pressure, while the other was submitted to low vacuum for 3 days, inside the Hall effect system.

The resistivity and carrier concentration remeasured 3 days later indicate there is a greater recovery of these initial parameters for the replica left at atmospheric pressure, in air, a medium containing higher oxygen levels than a low-vacuum ambient (Figure 27). If the vacuum had been higher, and the sample had been left for a longer time, it is expected that the difference in resistivity and carrier concentration would be even greater. In summary, this was a simple test that supports the presumed mechanism taking place during the UV-O_3 treatment.

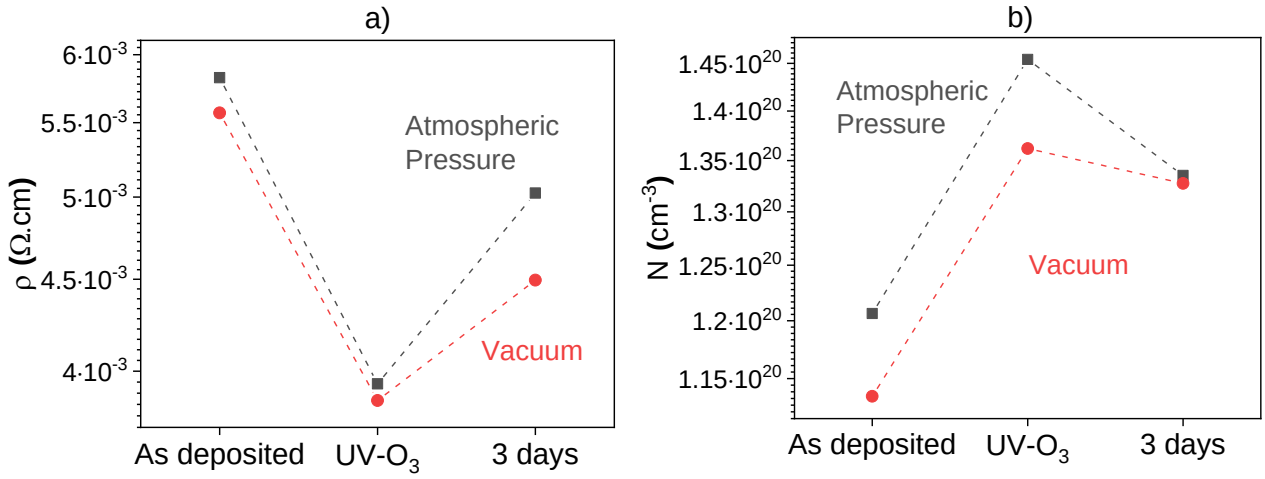

Figure 27: a) Resistivity and b) Carrier concentration of replicas of sample AZO180-129:1 as deposited, after 15 minutes of UV-O3 and remeasured 3 days later, one left at atmospheric pressure and the other left in low vacuum inside the hall effect system.

3.6.1.2 Rapid Thermal Annealing

For the RTA process, an inert atmosphere composition (N_2) was chosen, as well as a temperature of 300 ºC, a pressure of 100 or 999 mbar, and the duration was varied from 30 seconds to 10 minutes. Additionally, every RTA process used 500 sccm of N_2, and a heating ramp of 100 ºC/s.

In theory, RTA promotes the diffusion of interstitial aluminium donors in the ZnO matrix, causing Al^{3+} substitution of Zn^{2+} lattice sites, which increases the carrier concentration and decreases the resistivity [37]. The atmosphere composition highly influences the final electrical properties, in this case, N_2 is an inert atmosphere that is expected to prevent aluminium out-diffusion and dopant deactivation [37]. A short duration (30 s) can reveal better results because it minimizes the diffusion of zinc to the grain boundaries, the segregation of aluminium into secondary, more resistive Al_2O_3 and $ZnAl_2O_4$ phases, and also the entrapment of nitrogen atoms at the grain boundaries [37]. This last phenomenon may be causing the increase of resistivity with treatment duration observed for both AZO180-99:1 and AZO180-59:1 samples (Figure 28).

The higher inflation of resistivity for a lower pressure might be related to more favourable Zn, O and Al diffusion conditions, as described previously, which lead to the reduction of the carrier concentration (A.8). The mobility behaviour is difficult to explain, because when N increases μ can decrease due to enhanced ionized impurity scattering, but μ can also decrease alongside N due to aluminium dopant deactivation from diffusion into other phases. Additionally, mobility can be affected by grain size, film roughness, stresses, and other factors, that can change during an RTA process [37].

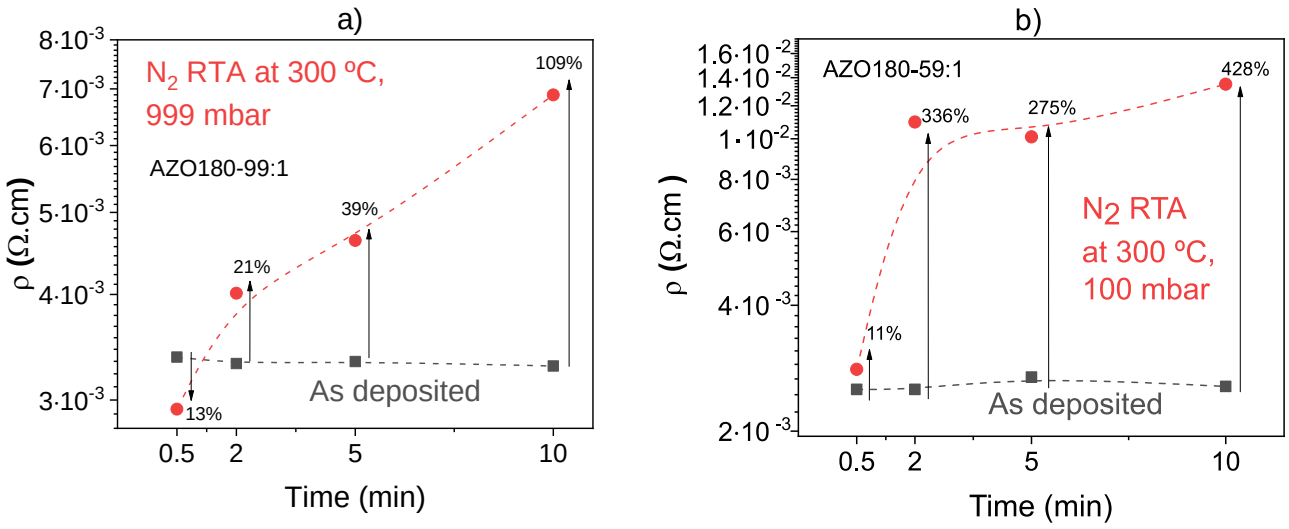

Figure 28: Resistivity as a function of N_2 RTA treatment time for a) AZO180-99:1 sample at 999 mbar, and b) AZO180-59:1 sample at 100 mbar.

3.7 Benchmarking of TiN and AZO Electrical properties

Figure 30 displays electrical resistivity as a function of deposition temperature, and it includes reported literature values, as well as the lowest resistivities obtained of AZO and TiN for each deposition temperature. Analysing the plot, it can be seen that while AZO's resistivity tends to decrease almost linearly with ALD deposition temperature (below 250 ºC, [16]), TiN's resistivity shows a less dependent relationship between these two parameters, as this process is enhanced by plasma, which provides extra energy for the chemical reactions taking place, without requiring as high a temperature as thermal ALD [2]. Regarding the samples produced in this work, the TiN stands out (blue circular shapes) by presenting considerably higher resistivity than the reported range. Contrarily, the AZO is within the usual range. As a result, the most conductive AZO sample (AZO180-59:1) presented a resistivity of 1.67×10^{-3} – 2.50×10^{-3} Ω.cm, which is below the most conductive TiN sample (300H20) with a resistivity of 3.07×10^{-3} Ω.cm.

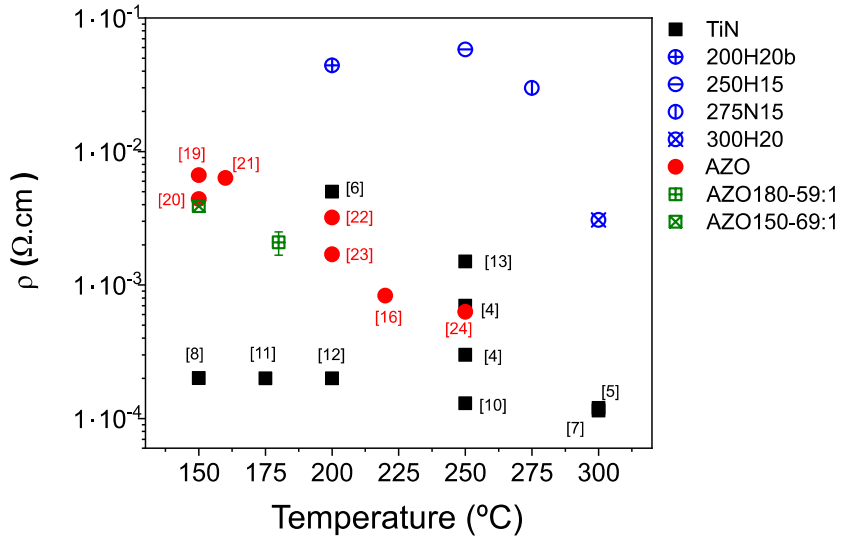

Figure 29: Resistivity as a function of deposition temperature. Includes TiN and AZO literature values, as well as the present work's lowest resistivities for each deposition temperature, blue for TiN and green for AZO.

3.8 Conformality Study

3.8.1 TiN Conformality

Polyimide patterned structures on glass (A.4) were used as substrates for the deposition of TiN thin films covered with a capping layer of Al_2O_3, at different deposition temperatures, 250 ºC and 300 ºC. The EDS elemental maps help understand the SEM images (Figure 30-Figure 31), by identifying the expected elements present in each material: Ti in the TiN, Al in the Al_2O_3, Si in the glass and C in the PI.

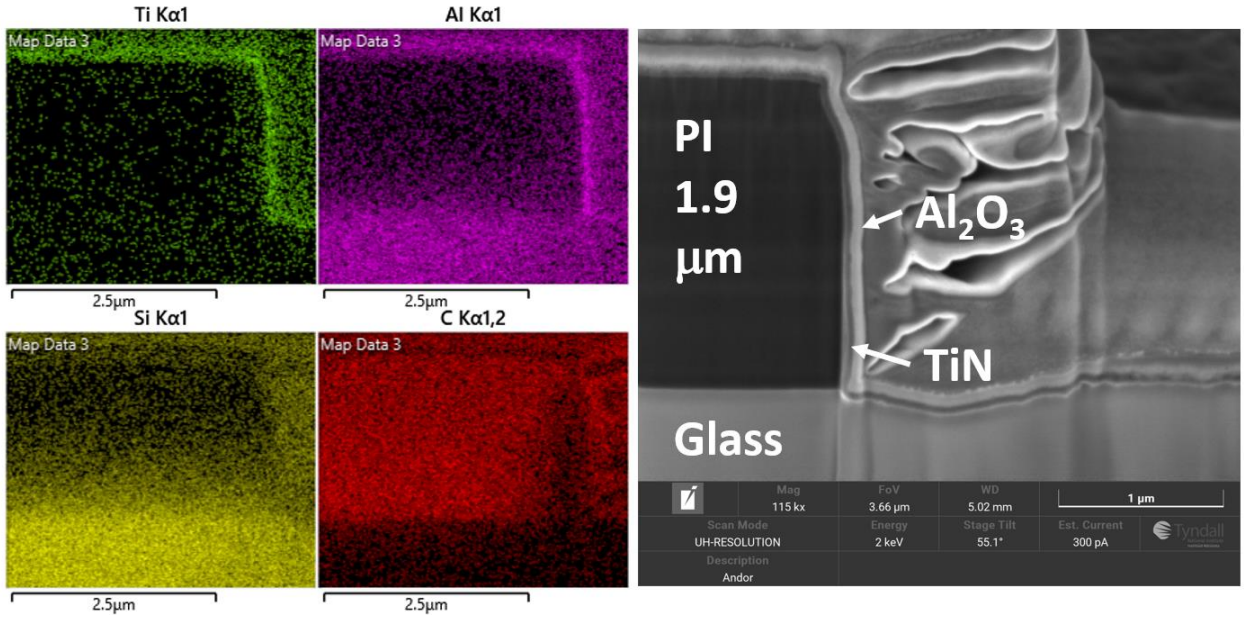

Figure 30: EDS elemental maps and SEM image of 600 cycles of TiN and 500 cycles of Al_2O_3 on a PI/glass step patterned substrate, at 250 ºC.

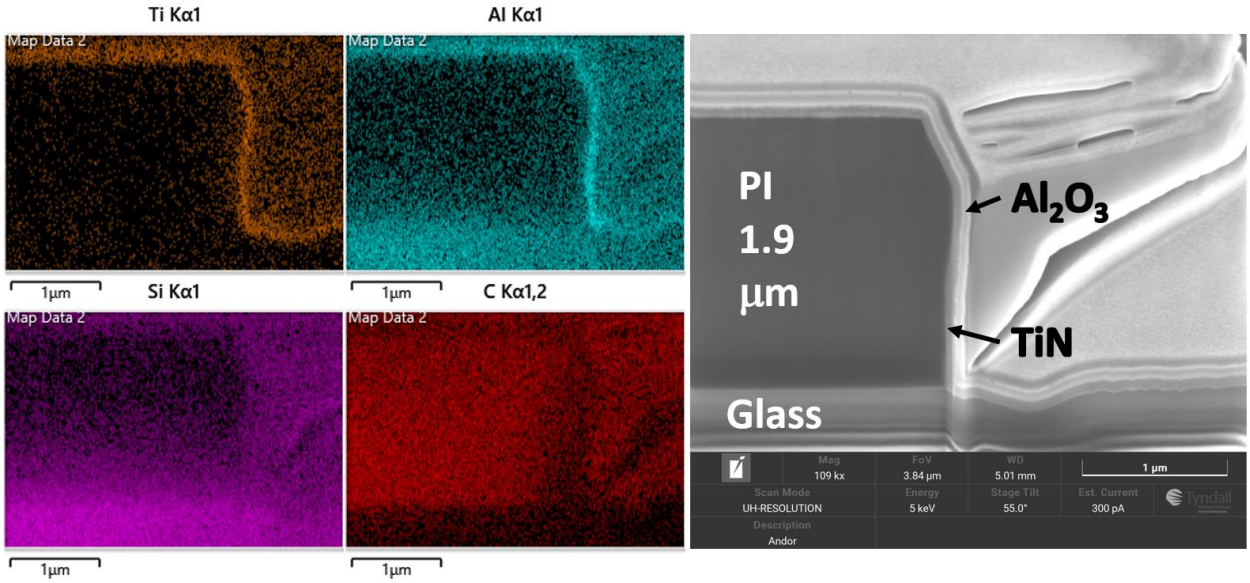

Figure 31: EDS elemental maps and SEM image of 600 cycles of TiN and 500 cycles of Al_2O_3 on a PI/glass step patterned substrate, at 300 ºC.

Both TiN thin films grew relatively uniformly over the PI and glass substrates, as visible by a less than 10% variance in thickness (Table 10). The conformality, it is estimated by dividing the thickness of the film grown on the side of the PI step, by the thickness of the film on top of the PI step, or on top of the glass. In this way, two conformality values can be obtained between the PI side and the PI top (PI/PI), and between the PI side and the glass top (PI/glass) for both TiN directly on these materials, and for the following Al_2O_3 layer.

These results point towards a higher conformality for the deposition at 250 ºC (>90%), compared with the higher temperature of 300 ºC (>75%) (Figure 32), which is consistent with the fact that CVD-like growth occurs to a higher extent, at elevated temperatures. On another note, the similar top thickness of the TiN grown on PI and on glass, for each depositing temperature, indicate a reasonable plasma uniformity. On the contrary, the Al_2O_3 layers grew very disparately, depending on the type of substrate, for unknown reasons. Potential explanations include intermixing of the Al_2O_3 with the TiN, which is visible on the PI top at 250 ºC, or else, an imperfect ion mill of the sample during its preparation, which resulted in a slight inclination, potentially distorting the SEM cross-section.

Table 10: Thickness measurements of TiN and Al_2O_3 layers from SEM images.

T (ºC)	**250**		**300**	
Substrate	**PI**	**Glass**	**PI**	**Glass**
TiN top (nm)	48.0 ± 1.8	47.2 ± 3.6	70.3 ± 2.4	70.1 ± 2.9
TiN side (nm)	48.5 ± 2.9	-	58.9 ± 6.3	-
Al_2O_3 Top (nm)	99.1 ± 3.4	62.9 ± 1.6	100.2 ± 3.4	82.8 ± 4.1
Al_2O_3 side (nm)	63.8 ± 3.0	-	64.5 ± 3.0	-

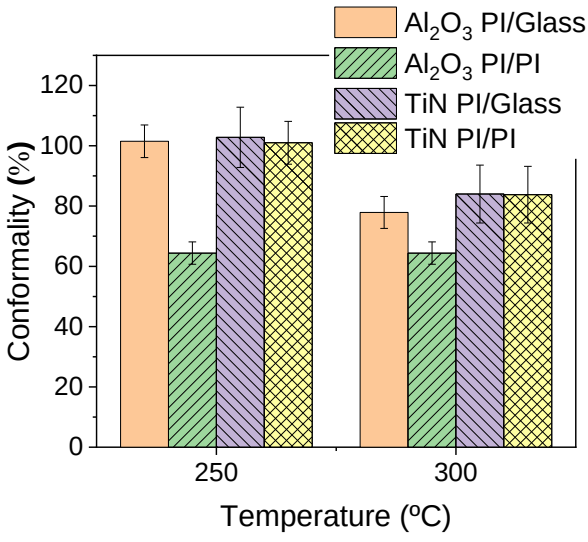

Figure 32: Conformality of Al_2O_3 and TiN layers as a function of substrate and temperature.

3.8.2 AZO Conformality

AZO thin films were grown on the PI/glass substrates by thermal ALD at two distinct deposition temperatures and DEZ:TMA ratios, namely the conditions of samples AZO150-69:1 and AZO180-59:1 (Figure 33 a) and b)). Exceptionally, these depositions took place at Tyndall National Institute, using the *Picosun* reactor, instead of the *Beneq* reactor used thus far for the AZO process. As such the recipe had to be adjusted to comply with the system restrictions (A.3). Additionally, the number of deposition cycles was increased (980 for the PAZO150-69:1 and 960 for the PAZO180-59:1) to get a thick enough film to more effectively examine its conformality.

In this case, both temperatures showed very high uniformity, with less than 2% variance of thickness (Table 11), and conformality above 90% for both deposition temperatures (Figure 34), expected from a controlled thermal ALD process [2].

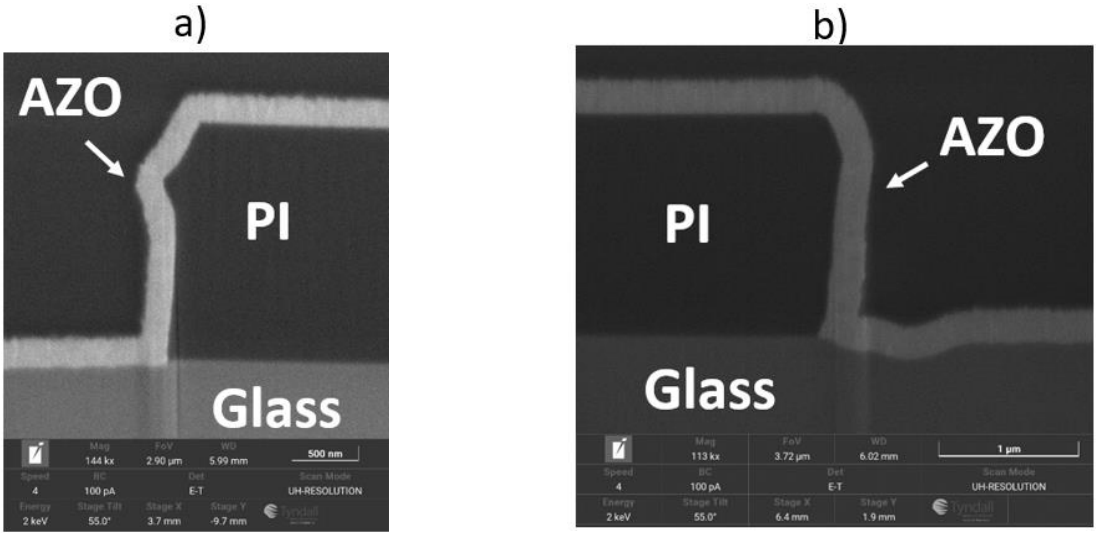

Figure 33: SEM images of a) PAZO150-69:1 and b) PAZO180-59:1 deposited on PI/glass step patterned substrates.

Table 11: Thickness of AZO films measured from SEM images.

T (ºC)	150		180	
Substrate	**PI**	**Glass**	**PI**	**Glass**
AZO top (nm)	211.5 ± 1.6	215.8 ± 2.3	233.4 ± 2.6	228.9 ± 1.9
AZO side (nm)	197.5 ± 3.3	-	219.5 ± 1.2	-

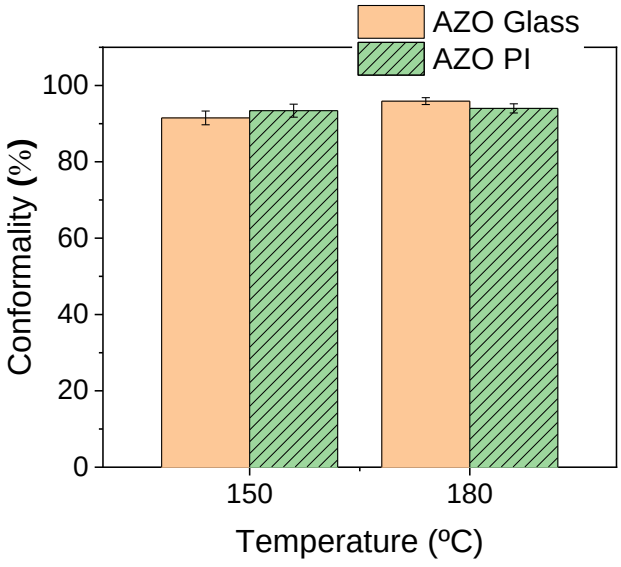

Figure 34: Conformality of AZO as a function of substrate and temperature.

3.8.3 Final considerations on TiN and AZO conformality

At this stage it is possible to compare two different materials deposited by different methods on equal substrates. Regarding thin film uniformity along the full substrate surface area, the AZO showed the best results, with a lower relative thickness error. Moreover, both materials grew, individually, at the same GPC on both PI and glass substrates, proving to be compatible with PI. Concerning the actual conformality, both materials presented above 90% for these substrates, however the AZO's error was much lower, and considering the difference in deposition temperature, from 150/180 ºC for the AZO, to 250 ºC for the TiN, it makes the AZO a more suitable choice to conformally coat a complex and temperature sensible structure, such as a polyimide flexible device. In reality, these substrates presented a very simple geometry with PI steps of less than 2 µm, not reaching the limit of what can be achieved by both PEALD and thermal ALD, namely conformality to high aspect ratio trenches, or nanostructures such as carbon nanotubes.

4. CONCLUSIONS AND FUTURE WORK

The goal of this work was to develop PEALD and ALD processes of TiN and AZO conductive thin films to, ultimately, study their conformality to polyimide patterned substrates, presenting a novel possibility for the application as electrical contacts and interconnection layers in flexible electronic devices.

The optimized conditions for the TiN deposition process were the shorter precursor pulse of TDMAT, 0.3 s, the longest plasma pulse, 20 s, a H_2/N_2 plasma rather than N_2, and the highest temperature tested, 300 ºC. These conditions provided the least resistive sample of this material, with a resistivity of 3.07×10^{-3} Ω.cm. This is within the upper limit of the reported literature values, because of high carbon and oxygen contamination, as observed from XPS depth profile measurements. The attributed cause was a high CVD-like growth resulting from precursor thermal decomposition, which lead to a high carbon contamination, in the form of unstable C-H bonds, contributing to the formation of a porous structure, and efficiently incorporating oxygen, from exposure to air. The oxygen occupied nitrogen vacancies, diminishing the number of Ti-N bonds in view of Ti-O bonds. It is important to note the reactor pressure used in the PEALD depositions, 4.5 Torr, was considerably higher than those reported, from 1 mTorr to 1 Torr, and this provokes a decrease of the onset temperature of thermal decomposition of the precursor, strongly influencing the final film composition and electrical properties.

For future perspectives, the precursor pulse should be kept short along with a lower reactor pressure, to produce denser films, containing less carbon and oxygen impurities. Moreover, a longer plasma duration should be investigated, as this parameter demonstrated great potential to reduce resistivity, and pure H_2 plasma could also be tested. A thickness series with more points should also be conducted to access GPC behaviour and facilitate detection of nucleation delay and other non-optimal growth phenomena. Regarding film characterization, the thickness and density could be measured using X-ray Reflectivity, which would help confirm the proposed conclusion regarding the samples' structure.

Thermal ALD using DEZ, TMA and water precursors at 180 ºC allowed the fabrication of the lowest resistivity (1.67×10^{-3} Ω.cm), polycrystalline thin film of AZO, by effectively doping ZnO with 1.94% atomic aluminium, as measured by EDS. Samples deposited at a temperature of 180 ºC demonstrated better electrical properties relative to those produced at 150 ºC, which is related to an enhanced removal of precursor ligands at higher temperatures. The aluminium doping concentrations measured between samples with different DEZ:TMA ALD cycle ratios were extremely close, 1.76% - 1.94%, and just below the reported range for the most conductive AZO films, 1.9% - 3.0%. This suggests that, in the future, additional samples should be deposited with lower DEZ:TMA ratio in order to reach the optimal %Al, and consequently the lowest resistivity of as deposited films, before resorting to post-treatments. Furthermore, instead of the traditional super cycle sequence of n cycles of ZnO followed by one cycle of Al_2O_3, different pulse sequences could also be studied [18,24]. In addition, XPS measurements could be used to acquire more accurate aluminium dopant concentrations, as well as information regarding the incorporation of precursor in the AZO films as a function of deposition temperature.

A 15-minute-long UV-O_3 post-treatment proved to be effective in temporarily improving the AZO's electrical properties by decreasing its resistivity. The proposed mechanism was the removal of oxygen from the film, increasing the number of oxygen vacancies, and consequently, the carrier concentration. This was tested when a sample was left in low vacuum for 3 days after being submitted to a 15-minute UV-O_3 treatment. This sample showed a lower recovery of both resistivity and carrier concentration, compared with a sample left in atmospheric pressure. In short, if the deposited film is encapsulated with a material that does not contain oxygen, after a UV-O_3 treatment, before exposure to air, the improved electrical properties may be retained.

Henceforth it would be interesting to apply this procedure to the TiN films to explore the removal of excess oxygen in this material's structure and, afterwards, analyse its electrical behaviour.

Conformality was studied by growing TiN films at 250 ºC and 300 ºC, as well as AZO films at 150 ºC and 180 ºC, on patterned steps of polyimide on glass substrates. SEM images revealed an above 90% conformality for both AZO samples and for the lower temperature TiN sample, and above 75% for the higher temperature. Besides, the measured thickness of all films grown on the polyimide was similar to the part of the films grown directly on the glass for different deposition temperatures, indicating good growth compatibility of TiN and AZO on this flexible material. Subsequently other more complex high aspect ratio structures such as trenches, or carbon nanotubes should be used for a stricter conformality test of the thin films. Perhaps then a clearer difference between the conformality obtained with PEALD of TiN and ALD of AZO would be observed.

Finally, when compared side by side, the AZO demonstrated better electrical and structural performance using lower thermal budget, being the best choice among these two materials for a future application as an electrical contact or interconnection in polyimide flexible electronic devices.

5. REFERENCES

[1] Wong W S 2009 *Flexible Electronics* vol 11, ed W S Wong and A Salleo (Boston, MA: Springer US)

[2] Knoops H C M, Potts S E, Bol A A and Kessels W M M 2015 Atomic Layer Deposition *Handbook of Crystal Growth* ed T Kuech (Elsevier) pp 1101–34

[3] Mallick B C, Hsieh C, Yin K-M, Gandomi Y A and Huang K 2019 Review—On Atomic Layer Deposition: Current Progress and Future Challenges *ECS J. Solid State Sci. Technol.* **8** N55–78

[4] Kim J Y, Seo S, Kim D Y, Jeon H and Kim Y 2004 Remote plasma enhanced atomic layer deposition of TiN thin films using metalorganic precursor *J. Vac. Sci. Technol. A Vacuum, Surfaces, Film.* **22** 8–12

[5] Krylov I, Zoubenko E, Weinfeld K, Kauffmann Y, Xu X, Ritter D and Eizenberg M 2018 Obtaining low resistivity (∼100 μ Ω cm) TiN films by plasma enhanced atomic layer deposition using a metalorganic precursor *J. Vac. Sci. Technol. A Vacuum, Surfaces, Film.* **36** 051505

[6] Badie C, Tissot H, Sciacca B, Barr M K, Bachmann J, Vallée C, Gautier G, Defforge T, Astie V, Decams J-M, Bechelany M and Santinacci L 2023 Conductive TiN thin films grown by plasma-enhanced atomic layer deposition: Effects of N-sources and thermal treatments *J. Vac. Sci. Technol. A* **41** 032401

[7] Krylov I, Xu X, Zoubenko E, Weinfeld K, Boyeras S, Palumbo F, Eizenberg M and Ritter D 2018 Role of reactive gas on the structure and properties of titanium nitride films grown by plasma enhanced atomic layer deposition *J. Vac. Sci. Technol. A Vacuum, Surfaces, Film.* **36** 06A105

[8] Caubet P, Blomberg T, Benaboud R, Wyon C, Blanquet E, Gonchond J-P, Juhel M, Bouvet P, Gros-Jean M, Michailos J, Richard C and Iteprat B 2008 Low-Temperature Low-Resistivity PEALD TiN Using TDMAT under Hydrogen Reducing Ambient *J. Electrochem. Soc.* **155** H625

[9] Elam J W, Schuisky M, Ferguson J D and George S M 2003 Surface chemistry and film growth during TiN atomic layer deposition using TDMAT and NH3 *Thin Solid Films* **436** 145–56

[10] Shin J W, Lee J, Kim K, Kwon C, Park Y Bin, Park H, Kim K, Ahn H S, Shim D and An J 2022 Effect of nitrogen plasma on the mechanical and electrical properties of plasma-enhanced atomic layer deposited TiN films *Ceram. Int.* **48** 25651–5

[11] Kim D-H, Kim Y J, Park J-H and Kim J H 2004 Preparation of TiN films by plasma assisted atomic layer deposition for copper metallization *Mater. Sci. Eng. C* **24** 289–91

[12] Samal N, Du H, Luberoff R, Chetry K, Bubber R, Hayes A and Devasahayam A 2013 Low-temperature (≤200 ° C) plasma enhanced atomic layer deposition of dense titanium nitride thin films *J. Vac. Sci. Technol. A Vacuum, Surfaces, Film.* **31** 01A137

[13] Kim J Y, Kim D Y, Park H O and Jeon H 2005 Characteristics and Compositional Variation of TiN Films Deposited by Remote PEALD on Contact Holes *J. Electrochem. Soc.* **152** G29

[14] Lim S J, Kwon S and Kim H 2008 ZnO thin films prepared by atomic layer deposition and rf sputtering as an active layer for thin film transistor *Thin Solid Films* **516** 1523–8

[15] Ellmer K 2001 Resistivity of polycrystalline zinc oxide films: current status and physical limit *J. Phys. D. Appl. Phys.* **34** 3097–108

[16] Wu Y, Cao F and Ji X 2020 Optical and electrical properties of Al-doped ZnO thin films by atomic layer deposition *J. Mater. Sci. Mater. Electron.* **31** 17365–74

[17] Weckman T and Laasonen K 2018 Atomic Layer Deposition of Zinc Oxide: Study on the Water Pulse Reactions from First-Principles *J. Phys. Chem. C* **122** 7685–94

[18] Gao Z and Banerjee P 2019 Review Article: Atomic layer deposition of doped ZnO films *J. Vac. Sci. Technol. A Vacuum, Surfaces, Film.* **37**

[19] R. Felizardo 2021 *Aluminum doping of zinc oxide thin films produced by atomic layer deposition for transparent conductors* (FCT NOVA)

[20] Banerjee P, Lee W-J, Bae K, Lee S B and Rubloff G W 2010 Structural, electrical, and optical

properties of atomic layer deposition Al-doped ZnO films *J. Appl. Phys.* **108**

[21] Swatowska B, Powroźnik W, Czternastek H, Lewińska G, Stapiński T, Pietruszka R, Witkowski B S and Godlewski M 2021 Application Properties of ZnO and AZO Thin Films Obtained by the ALD Method *Energies* **14** 6271

[22] Lee D, Kim H, Kwon J, Choi H, Kim S and Kim K 2011 Structural and Electrical Properties of Atomic Layer Deposited Al-Doped ZnO Films *Adv. Funct. Mater.* **21** 448–55

[23] Lee D, Kwon J, Kim S-H, Kim H-M and Kim K 2011 Effect of Al Distribution on Carrier Generation of Atomic Layer Deposited Al-Doped ZnO Films *J. Electrochem. Soc.* **158** D277

[24] Bui Q C, Consonni V, Boubenia S, Gay G, Perret C, Zeghouane M, Labau S, Roussel H, Mescot X, Ardila G and Salem B 2023 High figure-of-merit in Al-doped ZnO thin films grown by ALD through the Al content adjustment *Materialia* **31** 101863

[25] Narayanan V, de Buysser K, Bruneel E and Driessche I van 2012 X-ray Photoelectron Spectroscopy (XPS) Depth Profiling for Evaluation of La2Zr2O7 Buffer Layer Capacity *Materials (Basel).* **5** 364–76

[26] Musschoot J, Xie Q, Deduytsche D, Van den Berghe S, Van Meirhaeghe R L and Detavernier C 2009 Atomic layer deposition of titanium nitride from TDMAT precursor *Microelectron. Eng.* **86** 72–7

[27] Prieto P and Kirby R E 1995 X-ray photoelectron spectroscopy study of the difference between reactively evaporated and direct sputter-deposited TiN films and their oxidation properties *J. Vac. Sci. Technol. A Vacuum, Surfaces, Film.* **13** 2819–26

[28] Krylov I, Qi Y, Korchnoy V, Weinfeld K, Eizenberg M and Yalon E 2020 Role of temperature on structure and electrical properties of titanium nitride films grown by low pressure plasma enhanced atomic layer deposition *J. Vac. Sci. Technol. A Vacuum, Surfaces, Film.* **38**

[29] Miikkulainen V, Leskelä M, Ritala M and Puurunen R L 2013 Crystallinity of inorganic films grown by atomic layer deposition: Overview and general trends *J. Appl. Phys.* **113**

[30] Kim J, Jung S-M, Kim K-S, You S-H, Lee B-J and Kim Y-T 2022 Highly Active Electrocatalyst based on Ultra-low Loading of Ruthenium Supported on Titanium Carbide for Alkaline Hydrogen Evolution Reaction *J. Electrochem. Sci. Technol.* **13** 417–23

[31] Shi J, Jiang B, Liu Z, Li C, Yan F, Liu X, Li H, Yang C, Dong D and Hao J 2021 Sputtered titanium nitride films on nanowires Si substrate as pseudocapacitive electrode for supercapacitors *Ceram. Int.* **47** 26758–67

[32] Hansen K, Cardona M, Dutta A and Yang C 2020 Plasma Enhanced Atomic Layer Deposition of Plasmonic TiN Ultrathin Films Using TDMATi and NH3 *Materials (Basel).* **13** 1058

[33] Ahn C H, Lee S Y and Cho H K 2013 Influence of growth temperature on the electrical and structural characteristics of conductive Al-doped ZnO thin films grown by atomic layer deposition *Thin Solid Films* **545** 106–10

[34] Vig J R 1985 UV/ozone cleaning of surfaces *J. Vac. Sci. Technol. A Vacuum, Surfaces, Film.* **3** 1027–34

[35] Xu Q, Cheng L, Meng L, Wang Z, Bai S, Tian X, Jia X and Qin Y 2019 Flexible Self-Powered ZnO Film UV Sensor with a High Response *ACS Appl. Mater. Interfaces* **11** 26127–33

[36] Petrova D, Napoleonov B, Minh C N H, Marinova V, Lan Y, Avramova I, Petrov S, Blagoev B, Videva V, Strijkova V, Kostadinov I, Lin S and Dimitrov D 2023 The Effect of Post Deposition Treatment on Properties of ALD Al-Doped ZnO Films *Nanomaterials* **13** 800

[37] Ayachi B, Aviles T, Vilcot J and Sion C 2016 Rapid thermal annealing effect on the spatial resistivity distribution of AZO thin films deposited by pulsed-direct-current sputtering for solar cells applications *Appl. Surf. Sci.* **366** 53–8

APPENDIX

A.1 TiN PEALD Recipe Information

Table 12: ALD conditions on the *R200 Advanced Picosun* system.

Layer	TiN	TiN	TiN	Al_2O_3
T (ºC)	250; 275; 300	250; 275; 300	200; 250; 300	*
Precursor	TDMAT			TMA
Precursor Pulse (s)	0.3		2	0.1
Precursor Purge (s)	10			
Bottle T (˚C)	85-90			20
Neck T (˚C)	100-110			60-100
Co-reactant Carrier Gas	N_2			
Co-reactant Carrier Gas Flow (sccm)	120		600 (w/ booster)	120
Co-reactant Purge (s)	5			10
Plasma Power (W)	1800			-
Co-reactant	N_2	H_2/N_2 (1/10)		H_2O
Co-reactant Pulse (s)	10; 15; 20		20	0.1
Co-reactant Purge (s)	10			
Co-reactant Carrier Gas	Ar			N_2
Co-reactant Carrier Gas Flow (sccm)	100	110-120		120
Co-reactant Flow (sccm)	50	30-40		-
Reactor Pressure (hPa)	6		6-7	6
Number of Cycles	400		400; 600; 1000; 1500	variable

Notes: *The deposition temperature of any Al_2O_3 layer was always the same as its adjacent TiN layer.

A.2 AZO ALD Recipe

*Recipe for AZO
*Precursors DEZ, TMA and Water by own vapor pressures
*FCT, 2021 1 Oct
*Based on flow chart N503256
*DEZ at liquid source 3
*TMA at liquid source 2
*Water at liquid source 4

*Program start
SPROG

*Close Glove box valve
CLOSE DV-GB1

*Open the N2 main valve and chamber flow valve and make sure filling valve is closed
OPEN DV-SN1,DV-NV2
CLOSE DV-NV1

*Open main vacuum valve
OPEN DV-VP1

*Set flows
FLOW MFC-NOVS=250
FLOW MFC-NOPS=600

*Close pulse valves
CLOSE DV-PL1,DV-BL1
CLOSE DV-PL2,DV-BL2
CLOSE DV-PL3,DV-BL3
CLOSE DV-PL4,DV-BL4
CLOSE DV-PH1,DV-BH1,DV-BHA1

CLOSE DV-PH2,DV-BH2,DV-BHA2
CLOSE DV-PH3,DV-BH2,DV-BHA3

*Close process gas valves
CLOSE DV-PN1
CLOSE DV-PG1
CLOSE DV-PG7,DV-PG8
CLOSE DV-PG1C
*Check the vacuum level
WUNTIL PT-P1<10 10s

*Set temperatures
TEMP TE-R1S=150 (variable)

*wait until temperature is ok
WUNTIL TE-R1<TE-R1S 5h

*Are temperatures ok to start the process?
WRITE M5
WUSER YES

*open precursor hand valves
WRITE M6
WUSER YES

*Pulsing

REPEAT 3 (variable)
REPEAT 129 (variable)
Pulse DV-PL3 500ms

Purge 10s
Pulse DV-PL4 150ms
Purge 10s
REND
REPEAT 1 (variable)
Pulse DV-PL2 150ms
Purge 10s
Pulse DV-PL4 150ms
Purge 10s
REND
REND

*Set temperatures
TEMP TE-R1S=10

*Close pulse valves
CLOSE DV-PL1,DV-BL1
CLOSE DV-PL2,DV-BL2
CLOSE DV-PL3,DV-BL3
CLOSE DV-PL4,DV-BL4
CLOSE DV-PH1,DV-BH1,DV-BHA1
CLOSE DV-PH2,DV-BH2,DV-BHA2
CLOSE DV-PH3,DV-BH3,DV-BHA3

*Close process gas valves
CLOSE DV-PN1
CLOSE DV-PG1
CLOSE DV-PG7,DV-PG8
CLOSE DV-PG1C

*close precursor hand valves

WRITE M7
WUSER YES

*confirm that all precursor hand valves are closed
WRITE M22
WUSER YES

*Start line purge
WRITE M39
WUSER YES

PULSE DV-BL3 10min
PULSE DV-PL3 10min
PULSE DV-BL2 10min
PULSE DV-PL2 10min

*end program
EPROG

A.3 Sample List

Table 13: List of samples deposited by PEALD and ALD.

Sample	**Description** (the order of the layers is from the substrate to the outmost surface layer)
300N10	200 cycles Al_2O_3; 400 cycles TiN, 10 s of N_2 plasma, 300 ˚C
300N15	200 cycles Al_2O_3; 400 cycles TiN, 15 s of N_2 plasma, 300 ˚C
300N20	200 cycles Al_2O_3; 400 cycles TiN, 20 s of N_2 plasma, 300 ˚C
250N15	200 cycles Al_2O_3; 400 cycles TiN, 15 s of N_2 plasma, 250 ˚C
275N15	200 cycles Al_2O_3; 400 cycles TiN, 15 s of N_2 plasma, 275 ˚C
300H10	200 cycles Al_2O_3; 400 cycles TiN, 10 s of H_2/N_2 plasma, 300 ˚C
300H15	200 cycles Al_2O_3; 400 cycles TiN, 15 s of H_2/N_2 plasma, 300 ˚C
300H20	200 cycles Al_2O_3; 400 cycles TiN, 20 s of H_2/N_2 plasma, 300 ˚C
250H15	200 cycles Al_2O_3; 400 cycles TiN, 15 s of H_2/N_2 plasma, 250 ˚C
275H15	200 cycles Al_2O_3; 400 cycles TiN, 15 s of H_2/N_2 plasma, 275 ˚C
Al_2O_3	200 cycles Al_2O_3 300 ˚C
300H20b	50 cycles Al_2O_3; 400 cycles TiN, 20 s of H_2/N_2 plasma, 300 ˚C, w/ booster
300H20b-Capped	50 cycles Al_2O_3; 400 cycles TiN, 20 s of H_2/N_2 plasma, 300 ˚C, w/ booster; 20 cycles Al_2O_3 capping layer
300H20b-600	50 cycles Al_2O_3; 600 cycles TiN, 20 s of H_2/N_2 plasma, 300 ˚C, w/ booster
300H20b-1000	50 cycles Al_2O_3; 1000 cycles TiN, 20 s of H_2/N_2 plasma, 300 ˚C, w/ booster
300H20b-1500	50 cycles Al_2O_3; 1500 cycles TiN, 20 s of H_2/N_2 plasma, 300 ˚C, w/ booster
200H20b	50 cycles Al_2O_3; 400 cycles TiN, 20 s of H_2/N_2 plasma, 200 ˚C, w/ booster
250H20b	50 cycles Al_2O_3; 400 cycles TiN, 20 s of H_2/N_2 plasma, 250 ˚C, w/ booster
P300H20b-600	600 cycles TiN, 20s of H_2/N_2 plasma, 300 ˚C, w/ booster + 500 cycles Al_2O_3
P250H20b-600	600 cycles TiN, 20s of H_2/N_2 plasma, 250 ˚C, w/ booster + 500 cycles Al_2O_3
AZO150-59:1	59×7=413 DEZ/H_2O cycles, 7 TMA/H_2O cycles, 420 total cycles, 150 ºC
AZO150-69:1	69×6=414 DEZ/H_2O cycles, 6 TMA/H_2O cycles, 420 total cycles, 150 ˚C
AZO150-79:1	79×5=395 DEZ/H_2O cycles, 5 TMA/H_2O cycles, 400 total cycles, 150 ˚C
AZO150-99:1	99×4=396 DEZ/H_2O cycles, 4 TMA/H_2O cycles, 400 total cycles, 150 ˚C
AZO150-129:1	129×3=387 DEZ/H_2O cycles, 3 TMA/H_2O cycles, 390 total cycles, 150 ˚C
AZO180-59:1	59×7=413 DEZ/H_2O cycles, 7 TMA/H_2O cycles, 420 total cycles, 180 ˚C
AZO180-69:1	69×6=414 DEZ/H_2O cycles, 6 TMA/H_2O cycles, 420 total cycles, 180 ˚C
AZO180-79:1	79×5=395 DEZ/H_2O cycles, 5 TMA/H_2O cycles, 400 total cycles, 180 ˚C
AZO180-99:1	99×4=396 DEZ/H_2O cycles, 4 TMA/H_2O cycles, 400 total cycles, 180 ˚C
AZO180-129:1	129×3=387 DEZ/H_2O cycles, 3 TMA/H_2O cycles, 390 total cycles, 180 ˚C
PAZO150-69:1	69×14=966 DEZ/H_2O cycles, 14 TMA/H_2O cycles, 980 total cycles, 150 ˚C on poly-imide/glass substrate. 0.2 s DEZ pulse instead of 0.5 s.
PAZO180-59:1	59×16=944 DEZ/H_2O cycles, 16 TMA/H_2O cycles, 960 total cycles, 180 ˚C on poly-imide/glass substrate. 0.2 s DEZ pulse instead of 0.5 s.

A.4 Polyimide Substrates

Polyimide films were fabricated by spin-coating a liquid adhesion promotor, VM652 (HDmicrosystems) on top of a glass substrate at 3000 rpm for 30 s, blow drying the substrate's backside and topside with a nitrogen spray gun, afterwards, spreading the polyimide for 1 minute followed by a soft-bake process of 90 s at 90 ˚C, letting it cool, and finally, a cure ramp of 240 ºC/h from 150 ºC to 350 ºC, leaving in 350 ºC for 30 minutes, for a total ramp time of 80 min. The final structure formed a solid PI layer of approximately 1.9 microns. These complexes of PI on glass were patterned by direct laser writing, with a *Heidelberg µPG 101 Tabletop Micro Pattern Generator*, to create trenches in the PI surface (Figure 35 - Figure 37). The patterning process consisted of depositing an aluminium layer over the PI, followed by the photoresist. The laser exposed the photoresist. Afterwards, the aluminium exposed areas were dry etched with 20 sccm of O_2 and 5 sccm of CF_4, along with the underlying PI, and finally, the remaining photoresist was removed by lifting off the aluminium layer. These polymer substrates were essential in the conformality study.

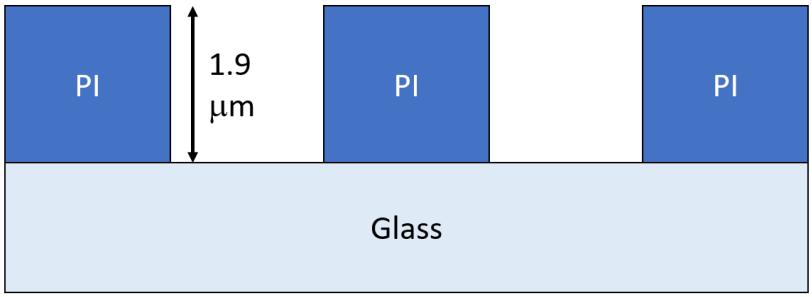

Figure 35: Representative image of the trench/step patterned PI on glass substrate.

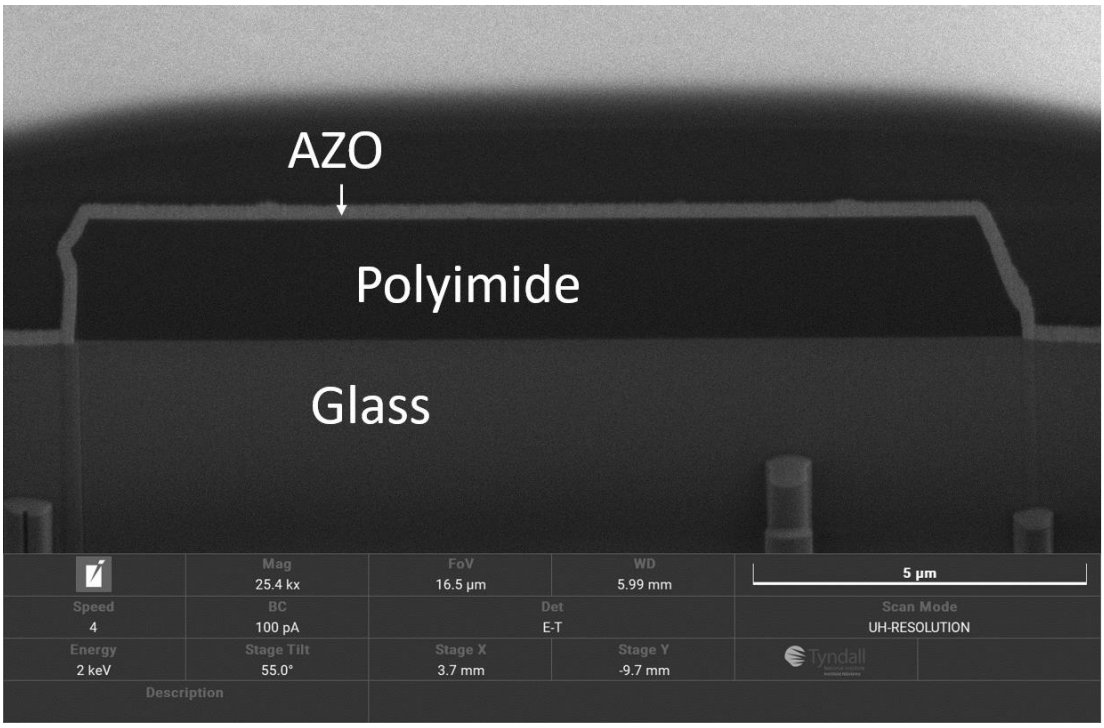

Figure 36: SEM image of a cross section of sample PAZO150-69:1.

Figure 37: SEM cross section image of a sample P250H20b-600.

A.5 TiN Thickness Calculation Method

Before beginning this analysis, the first three data points from the depth profile of sample 300H20b-Capped were removed because they contained information from the Al_2O_3 capping (Figure 9). This allowed a direct comparison of every measured sample, now with a similar initial surface composition. The method consisted in fitting the falling edge of the titanium XPS signal (Figure 38) and rising edge of the aluminium XPS signal (Figure 39), in each case using the same slope for every measured sample. The resulting fitting functions were intersected with the %Ti and %Al half maximum values [25], obtained from the maximum values present in Table 6. This part required the assumption that the %Al half maximum for booster samples was the same (9.6%), as well as the half maximum for the other samples (20.5%). The average of the intersection of the fitting functions with the %Ti and %Al was considered the sputter time necessary to reach the boundary between the TiN and the underlying Al_2O_3, and the difference between them was used to calculate the error of this method. This sputter time was directly associated with the thickness of the TiN in the capped sample, which allowed the extrapolation of the other samples' thickness.

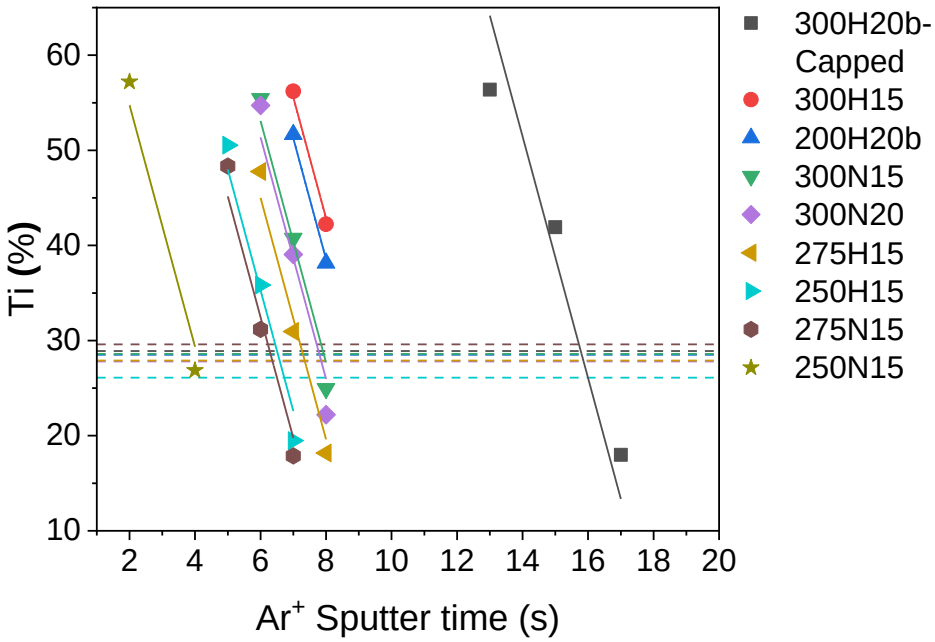

Figure 38: XPS Titanium signal as a function of Ar^+ sputter time, containing linear fittings with equal slope, and half maximum intersection dashed lines with corresponding colours.

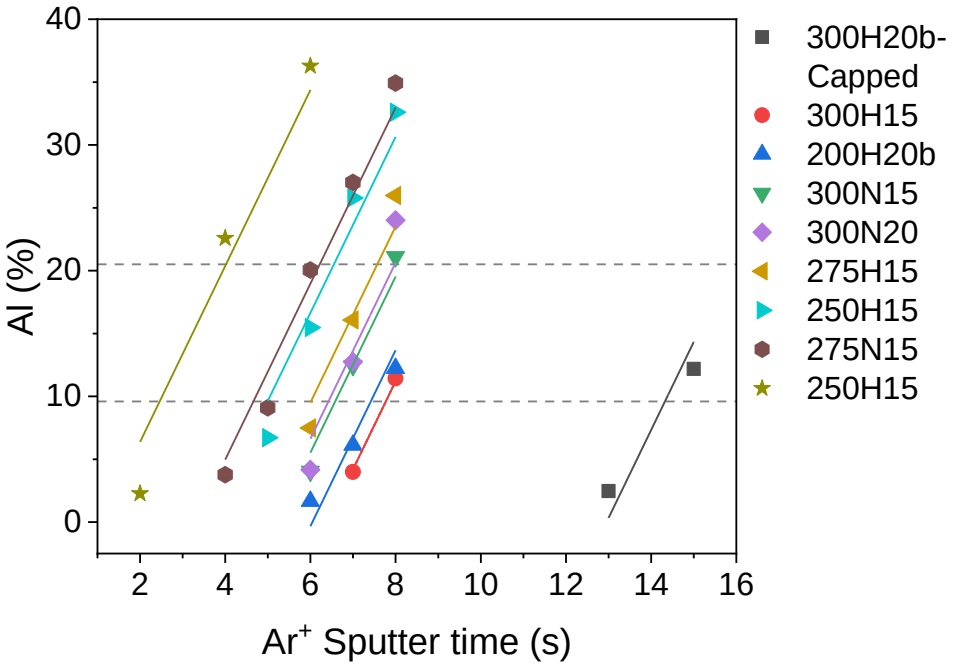

Figure 39: XPS Aluminium signal as a function of Ar^+ sputter time, containing linear fittings with equal slope, and half maximum intersection dashed lines at 9.6% and 20.5%.

A.6 XPS Models

The *casaxps* software was utilized in the analysis of the XPS results. The following model was adapted from numerous references that described the Ti 2p as a deconvolution of three duplet types of peaks [6]. Each duplet contains a 3/2 orbital, with a lower binding energy and a more intense signal, with well-defined peaks (low FWHM), and the 1/2 orbital, which is a higher binding energy orbital, with larger peaks (higher FWHM), restricted to have half the area of its 3/2 counterpart, as well as a specific binding energy offset, that decreases from metal states (6 eV) to oxide states (5.5eV), with the nitride states in the middle (5.85eV). As the literature does not specify the FWHM of the 1/2 orbitals, a restriction to a multiple of the FWHM of the 3/2 which minimized the residual standard deviation was chosen and applied to all Ti 2p results. Only the 3/2 Ti 2p components were used for the calculation of percentages of Ti bonds (%Ti-O, %Ti-N-O, %Ti-N) (Figure 40).

Nitrogen and carbon peaks were also evaluated with simpler models (Table 15). The N 1s peak in a titanium oxynitride contains three components, N-O-Ti and N-Ti-O have broad FWHM because they include many oxidized states, and N-Ti with a tighter FWHM [27]. After Ar^+ sputtering the C 1s peak at the sample surface reveals two clear components, C-H related with hydrocarbon bonds and C-Ti related with carbidic bonds from the precursor (Figure 41) [4].

The line shape for the components used was a mix of 70% Gaussian and 30% Lorentzian curves (GL(30)). A Shirley background type was used for the component peaks, and for the regions a Tougaard background was used. Region and component error bars were calculated directly with *casaxps*.

Table 14: XPS model for fitting of the Ti 2p peak with energy, area and FWHM restrictions.

Restrictions	**Ti-N**		**Ti-N-O**		**Ti-O**	
	A	**B**	**C**	**D**	**E**	**F**
	Ti 2p 3/2	**Ti 2p 1/2**	**Ti 2p 3/2**	**Ti 2p 1/2**	**Ti 2p 3/2**	**Ti 2p 1/2**
Binding Energy (eV)	454.91, 455.51	A + 5.85	456.02 - 456.62	C + 5.7	457.91 - 458.51	E + 5.5
Area		A × 0.5		C × 0.5		E × 0.5
FWHM (eV)	1.0 – 2.0	A × 1.4	1.0 – 2.0	C × 1.9	1.0 - 2.5	E × 1.9

Table 15: XPS model for fitting the N 1s and C 1s peak with energy, area and FWHM restrictions.

Restrictions	**N 1s**			**C 1s**	
	N-O-Ti	**N-Ti**	**N-Ti-O**	**C-H**	**C-Ti**
Binding Energy (eV)	399.00 - 400.00	397.11 - 397.31	396.30 - 396.50	284.8 - 285.1	281.9 - 282.1
FWHM (eV)	2.0 – 3.0	1.0 – 2.0	0.5 – 2.0	1.0 – 2.0	0.9 - 1.1

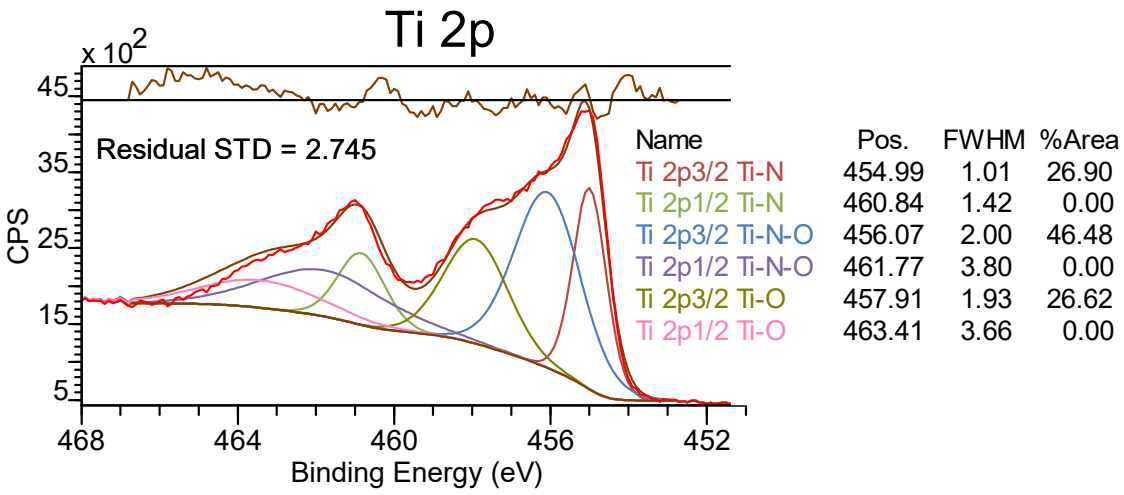

Figure 40: XPS Ti 2p detailed scan of sample 300H20b-Capped after 5 minutes of Ar^+ sputtering with 5 kV, using peak fitting with model described in Table 14. The raw data is in red, the components are identified in the table on the right, and together they form the envelope in brown.

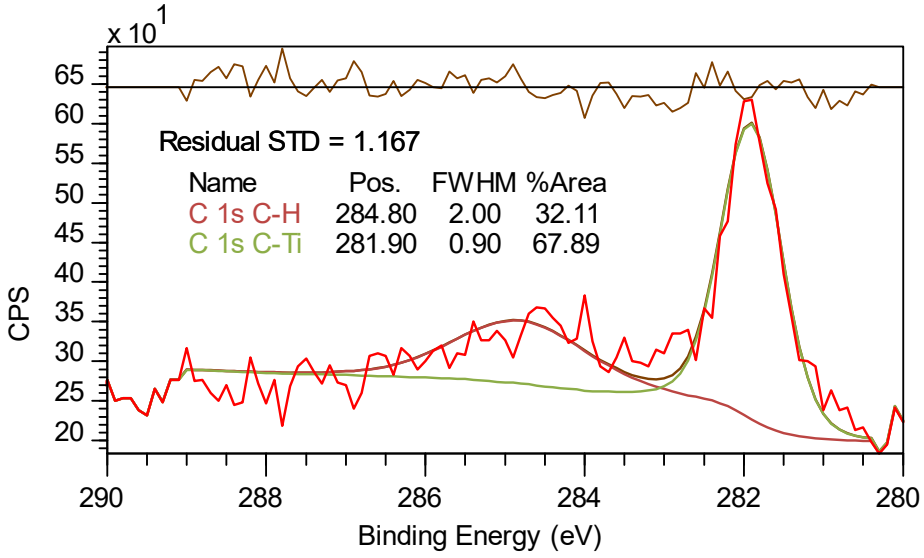

Figure 41: XPS C 1s detailed scan of sample 300H20b-Capped after 5 minutes of Ar^+ sputtering with 5 kV, using peak fitting with model described in Table 15. The raw data is in red, the components are identified in the table, and together they form the envelope in brown.

A.7 FIB-SEM

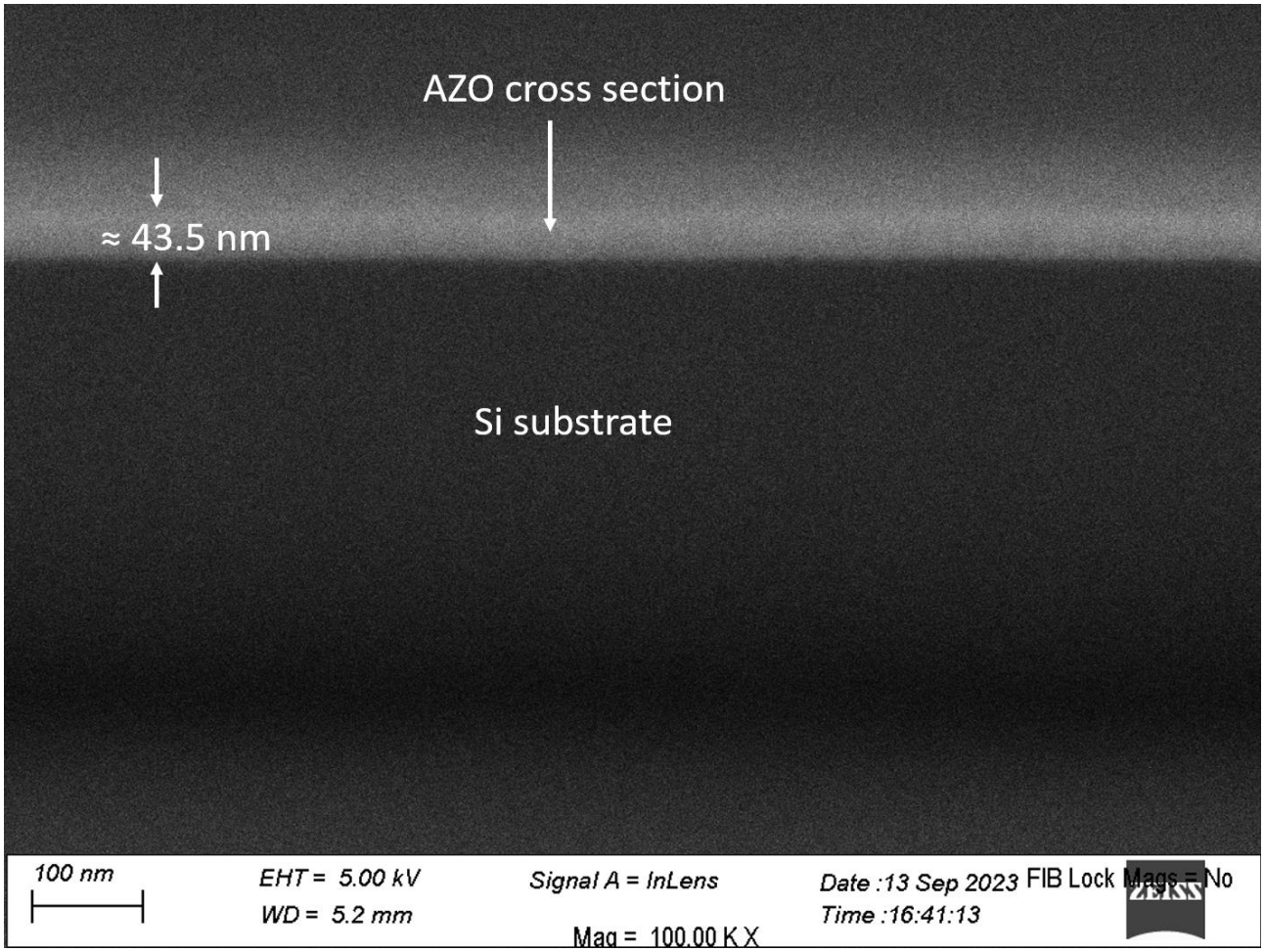

Figure 42: SEM image of a cross-section of sample AZO180-59:1 milled with FIB.

A.8 UV-Ozone and RTA post-treatment plots

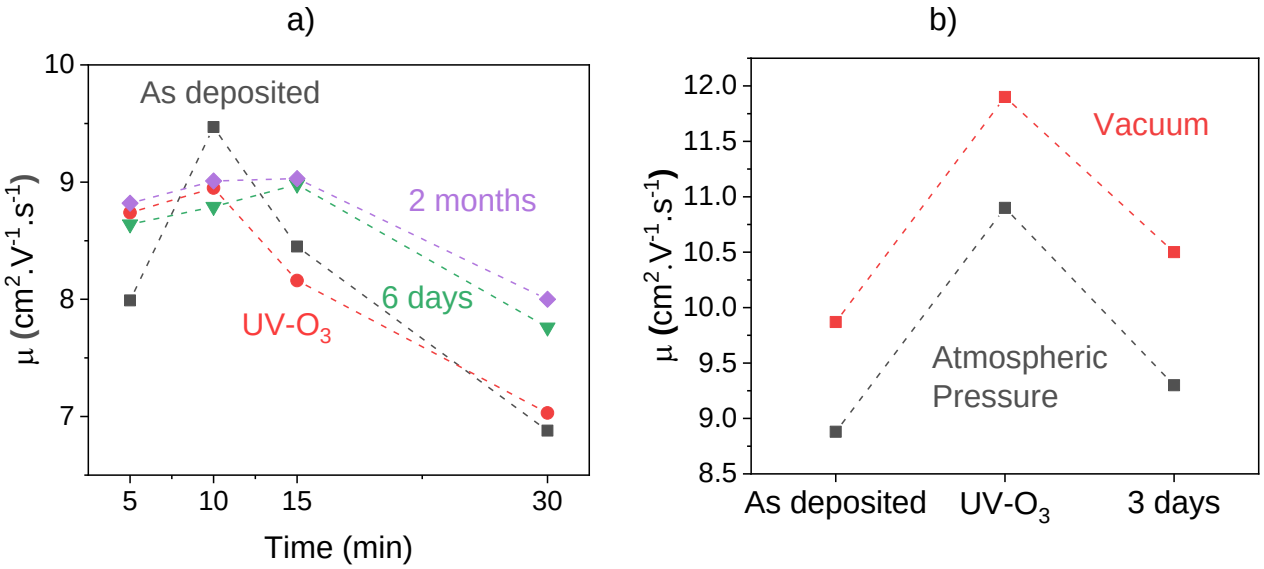

Figure 43: a) Mobility of AZO180-69:1 samples, as deposited, after UV-O_3 treatments of 5, 10, 15 and 30 minutes, remeasured 6 days and 2 months later, b) Mobility of AZO180-129:1 samples as deposited, after 15 min UV-O_3 post-treatment, and 3 days later.

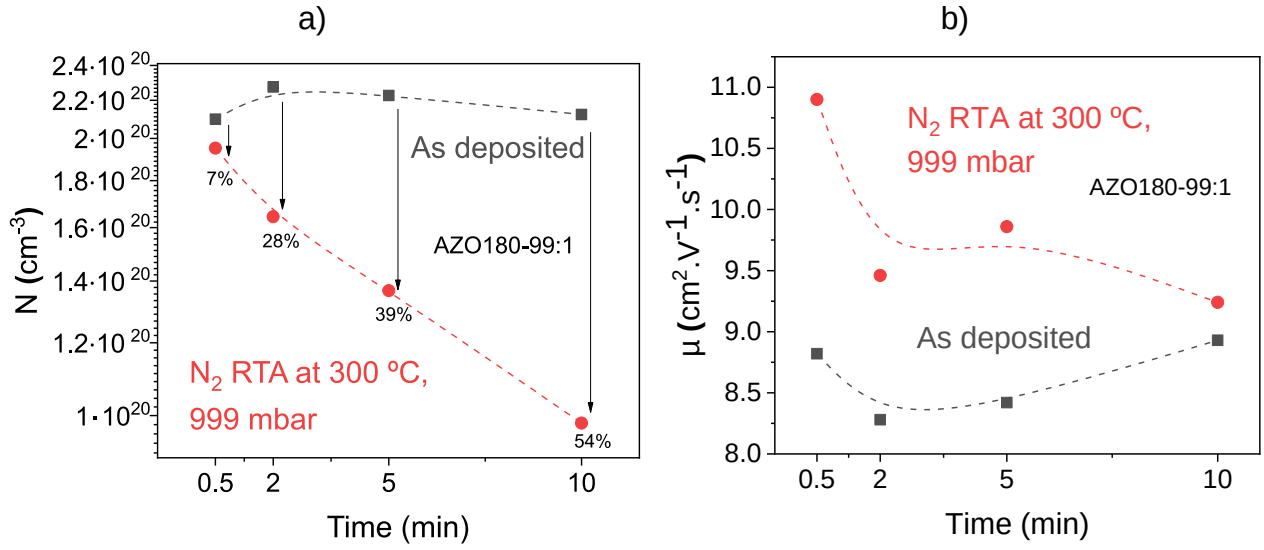

Figure 44: a) Carrier concentration and b) mobility of N_2 RTA post-treatments to sample AZO180-99:1, at 300 ºC and 999 mbar.